Mathematical Institute

Peter Julius Waldert, BSc BSc

Wolfson College

General Kernel Spectral Methods for Equilibrium Measures

MASTER'S THESIS

a thesis submitted for the degree of

Master of Science (MSc)

in

Mathematical Modelling and Scientific Computing (MMSC)

submitted to the

University of Oxford

Academic Supervisors

Dr. Timon Gutleb[a]

Prof. José A. Carrillo de la Plata[a]

[a]Mathematical Institute, University of Oxford

Oxford, August 2023

Abstract

What density distribution does a system of particles, a flock of birds or a school of fish approach in equilibrium? In this dissertation, we explore the construction of a spectral method for the solution of these particle density distributions $\hat{\rho}$, also referred to as *equilibrium measures*, on a d-dimensional ball of radius R. Our description generalises from animals to physical particles (atoms and molecules) by modelling their interaction through a pairwise interaction potential $K(r)$ that is only dependent on the distance r between two entities in the system. In the case of animals (so-called *active matter*), there is an additional term to model their self-propulsion. The spectral method is constructed using radial Jacobi polynomials $P_k^{(a,b)}$, which are orthogonal with respect to a certain weight function. They provide the basis for an N-term expansion of the solution and its coefficients are obtained through the solution of a linear system. By construction, the operators that appear are approximately banded and sparse, leading to a highly effective direct method for the solution of equilibrium measures to arbitrary precision.

Statement of Originality: The extension of the attractive-repulsive kernel spectral method into a general kernel spectral method along with an implementation of it is original. All code contributions, starting from the particle simulation software to the implementation of the spectral methods, are entirely original. We present a lemma for exact calculation of the support radius R when using an $N = 1$ order approximation of the solution and show that it is a unique minimiser. For higher orders, this result provides a solid initial guess for a subsequent optimisation routine.

Keywords: Pairwise Interaction Potentials, Many-Body Systems, Spectral Methods, Particle Simulations, Swarming Behaviour, Equilibrium Measures, Orthogonal Polynomials, Numerical Analysis

Implemented using: C++, Julia, Python

Acknowledgements

Contents

1

Introduction

In this present thesis we concern ourselves with many-body systems, treating particles in an abstract sense as they could take the form of physical atoms, birds in a flock or fish in a school. Other examples include ant colonies and swarms of insects such as locusts. A swarm of animals, a set of coordinated entities, brings many advantages for its members. For example, birds are able to minimise drag when travelling in a tightly packed group and it is easier to find a mate within the swarm than otherwise. They also mimic larger animals to fend off predators and swarming behaviour ("swarm intelligence") plays an important role in this process. There may be some disadvantages as well, like the accelerated spread of diseases (D'Orsogna 2017). In this thesis, we explore a method to describe this swarming behaviour and the patterns emerging from it mathematically, using pairwise interaction potentials.

From a perspective more rooted in physics, *pair potentials* $K : \mathbb{R}^+ \to \mathbb{R}$ provide a simple and computationally efficient way to approximate the interaction between two particles based solely on their distance (cf. Figures 1.1a and 1.1b as a simple illustration). Pairwise potentials can be used to approximate a wide range of interactions, including interatomic potentials in physics and computational chemistry. Examples of pair potentials include the Lennard-Jones potential and the Morse potential, which are widely used in molecular dynamics simulations to study the behaviour of atoms and molecules, as well as the Coulomb potential used to describe the interaction between two charges in electrodynamics.

From here on, we will refer to said swarm entities, be it fish, birds or atoms, as *particles.*
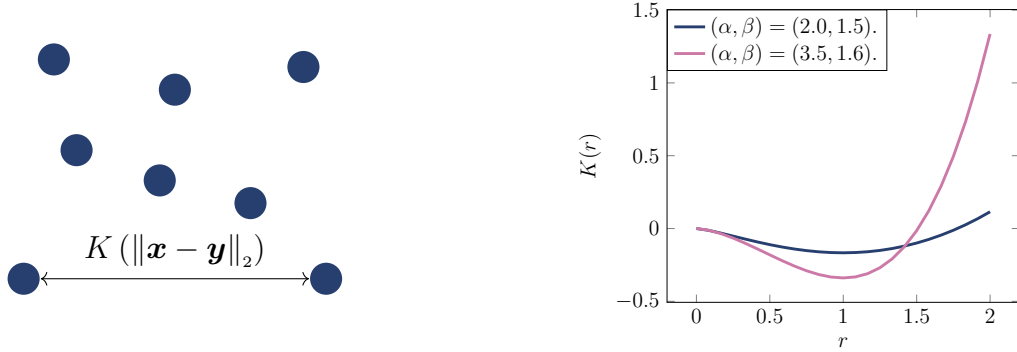
(a) $N_p = 8$ particles in open space interacting with one another through the pairwise potential $K(r)$ based on their distance r.

(b) Plot of attractive-repulsive potential functions $K_{\alpha,\beta}(r) = \frac{r^\alpha}{\alpha} - \frac{r^\beta}{\beta}$ for different α, β. More can be found in Figure 2.1.

Fractional differential operators act non-locally, contrary to a regular derivative which tells us local behaviour of a function at one point. Changes far away from that point do not affect a regular derivative, while they certainly do affect a fractional derivative such as the fractional Laplacian. In the context of solving Partial Differential Equations (PDEs) where equations are often set in terms of time, a helpful intuition can be to consider fractional derivatives as operators with "memory".

After providing a brief introduction to the setting of the problem considered in this dissertation along with motivation from a few biological and physical examples, we will now set up notational conventions.

1.1   Notational Conventions

Let $\mathbb{N}$ denote the natural numbers without 0 and let $\mathbb{N}_0 := \mathbb{N} \cup \{0\}$. In the following, we use capital letters, lowercase letters and **bold** lowercase letters to denote matrices, scalars and vectors, respectively. We frequently make use of the (Euclidean) 2-norm of a d-dimensional vector $\boldsymbol{x} \in \mathbb{R}^d$ with entries $x_1, ..., x_d \in \mathbb{R}$, as denoted by $\|\boldsymbol{x}\|_2 := \sqrt{\sum_{k=1}^d x_k^2}$. For readability, we use the notation $\boldsymbol{x}^2 := \boldsymbol{x}^T \boldsymbol{x} = \|\boldsymbol{x}\|_2^2 \in \mathbb{R}^+$. Let $\boldsymbol{e_1} := (1, 0, ..., 0)^T$ denote the unit vector in the direction of the first dimension. Let δ_{ij} denote the Kronecker delta, that is, $\delta_{ij} = 1$ when $i = j$ and 0 otherwise.

One should also clarify the nature of a few of the integrals appearing in this thesis which are often performed over the closed unit ball $B_1(\boldsymbol{x}) := \{\boldsymbol{y} \in \mathbb{R}^d \mid \|\boldsymbol{x} - \boldsymbol{y}\|_2 \leq 1\}$ centered at the origin $\boldsymbol{x} = \boldsymbol{0}$. These volume integrals (often ended by $\mathrm{d}^d y$ or $\mathrm{d}V$) over

the d-dimensional unit ball shall be written as

$$\int_{B_1(\mathbf{0})} \mathrm{d}\boldsymbol{y}\,,$$

where $\boldsymbol{y} \in \mathbb{R}^d$ is the integration variable. Note that some definitions of $B_1(\boldsymbol{x})$ are open sets, leaving out the shell $\{\boldsymbol{y} \in \mathbb{R}^d \mid \|\boldsymbol{x} - \boldsymbol{y}\|_2 = 1\}$. The choice of definition does not matter for our purposes as the shell, a hyperplane of Lebesgue measure 0, does not contribute to the integral.

All numerical plots and figures in this thesis were generated using the Makie visualisation tool (Danisch and Krumbiegel 2021), an open-source package available for the Julia computing language (Bezanson et al. 2017).

2

Particle Interaction Theory

This chapter will give a brief introduction to the theory of systems of pairwise-interacting particles, to pave the way for the upcoming discussion of numerical methods for the solution of their density distribution function.

2.1 A Many-Body System

An N_p-body system is a discrete set of particles with associated position $\boldsymbol{x_i} \in \mathbb{R}^d$ and velocity $\boldsymbol{v_i} := \frac{\mathrm{d}\boldsymbol{x_i}}{\mathrm{d}t} \in \mathbb{R}^d$ interacting with one another. Each particle individually is subject to inertia and its kinetic energy ("second moment" [1]) is given by

$$E_{\mathrm{kin},i} = \frac{\hat{\boldsymbol{p}}_{\boldsymbol{i}}^2}{2m} = \frac{(m\hat{\boldsymbol{v}}_{\boldsymbol{i}})^2}{2m} = \frac{1}{2}m \left\| \hat{\boldsymbol{v}}_{\boldsymbol{i}} \right\|_2^2 .$$

The second important ingredient is an interaction potential motivating pairwise forces $\boldsymbol{F_{ij}} \in \mathbb{R}^d$ between particles

$$\boldsymbol{F_{ij}} = -\nabla U_{ij} = - \left(\partial x_1, ..., \partial x_d \right)^T U_{ij} .$$

The total potential of a system of $N_p \geq 2$ particles $U \in \mathbb{R}$ can be calculated by summing up the pair potentials $U_{ij} \in \mathbb{R}$ between all pairs of particles

$$U = \sum_{i=1}^{N_p} \sum_{j=1, j \neq i}^{N_p} U_{ij} = \sum_{i=1}^{N_p} \sum_{j=1, j \neq i}^{N_p} K \left(\left\| \hat{\boldsymbol{x}}_{\boldsymbol{i}} - \hat{\boldsymbol{x}}_{\boldsymbol{j}} \right\|_2 \right) ,$$

where $\hat{\boldsymbol{x}}_{\boldsymbol{i}} \in \mathbb{R}^d$ represents the d-dimensional position of particle i, respectively.

---

[1] In kinetic theory, the 0th moment is the mass m_i of a particle, the first moment is the momentum $\hat{\boldsymbol{p}}_{\boldsymbol{i}}$ and the second moment is its kinetic energy $E_{kin,i}$.

In the absence of an external potential V, the total energy of the particle system is given by $E = E_{\text{kin}} + U$, so

$$E = \frac{1}{2} \sum_{i=1}^{N_p} m_i \hat{\boldsymbol{v}}_i^2 + \sum_{i=1}^{N_p} \sum_{j=1, j \neq i}^{N_p} K \left(\|\hat{\boldsymbol{x}}_i - \hat{\boldsymbol{x}}_j\|_2 \right) . \tag{2.1}$$

Following from Newton's equations of motion together with a model for friction and self-propulsion (cf. Section 2.4), each particle $i = 1, ..., N_p$ at position $\hat{\boldsymbol{x}}_i \in \mathbb{R}^d$ and time $t \in \mathbb{R}^+$ then follows

$$\frac{\mathrm{d}^2 \hat{\boldsymbol{x}}_i}{\mathrm{d}t^2} = f \left(\left\| \frac{\mathrm{d}\hat{\boldsymbol{x}}_i}{\mathrm{d}t} \right\|_2 \right) \frac{\mathrm{d}\hat{\boldsymbol{x}}_i}{\mathrm{d}t} - \frac{1}{N} \sum_{j=1, i \neq j}^{N} \nabla K \left(\|\hat{\boldsymbol{x}}_i - \hat{\boldsymbol{x}}_j\|_2 \right) , \tag{2.2}$$

for reference see, for example, Timon S. Gutleb, Carrillo and S. Olver 2022b; Timon S. Gutleb, Carrillo and S. Olver 2022a; Carrillo and Huang 2017. For now, we only consider the case without an external potential $V(\hat{\boldsymbol{x}})$.

2.2   Continuous Limit

The evolution equation (2.2) without friction or self-propulsion, in the mean-field limit as $N_p \to \infty$, becomes

$$\frac{\partial \hat{\rho}}{\partial t} = \nabla \cdot (\hat{\rho} \nabla K * \hat{\rho}) . \tag{2.3}$$

where $\hat{\rho} : \mathbb{R} \to \mathbb{R}$ is the particle density function and $*$ denotes a convolution. More details are given in Carrillo, Choi and Hauray 2014; Carrillo and Shu 2022. The solution $\hat{\rho}$ we are looking for within the scope of this dissertation is the *equilibrium measure* (cf. Definition 2.1), a particle density distribution function minimising the total potential U.

Definition 2.1: Equilibrium Measure

For a given pairwise interaction potential $K : \mathbb{R} \to \mathbb{R}$, the equilibrium measure $\hat{\rho} : D \to \mathbb{R}$ with $D \subseteq \mathbb{R}^d$ is a measure chosen such that

$$U_K[\hat{\rho}] := \frac{1}{2} \iint K \left(\|\hat{\boldsymbol{x}} - \hat{\boldsymbol{y}}\|_2 \right) \mathrm{d}\hat{\rho}(\hat{\boldsymbol{x}}) \, \mathrm{d}\hat{\rho}(\hat{\boldsymbol{y}}) ,$$

is minimised, where $\mathrm{d}\hat{\rho} = \hat{\rho}(\hat{\boldsymbol{x}}) \mathrm{d}\hat{\boldsymbol{x}}$.

Also consider the total mass of the equilibrium distribution, given by

$$M[\hat{\rho}] := \int \mathrm{d}\hat{\rho} = \int_{\text{supp}(\hat{\rho})} \hat{\rho}(\hat{\boldsymbol{x}}) \, \mathrm{d}\hat{\boldsymbol{x}} , \tag{2.4}$$

which, without loss of generality, we can choose to equal 1 to make $\hat{\rho}(\hat{\boldsymbol{x}})$ a *probability distribution*, which provides a useful interpretation of values of $\hat{\rho}$: The probability of finding a particle in a volume $\mathcal{V} \subseteq B_R(\mathbf{0})$ is given by $\int_{\mathcal{V}} \hat{\rho}(\boldsymbol{x})\,\mathrm{d}\boldsymbol{x}$. Also note that, as the integrand of the above integrals, we sometimes refer to the interaction potential $K(r)$ as an integral kernel or simply *kernel.*

Due to the absence of an external potential, solutions are translationally invariant, so for simplicity we can choose them to be centred at the origin. That is, on $D = B_R(\mathbf{0})$ instead of $B_R(\hat{\boldsymbol{x}}_{\text{centre}})$, where $\boldsymbol{x}_{\text{centre}} := \frac{1}{N_p} \sum_{i=1}^{N_p} \boldsymbol{x}_i$ with $R \in \mathbb{R}^+$ usually chosen as the smallest possible R such that $\text{supp}(\rho) \subseteq [-R, R]$.

As throughout the rest of this document, we restrict ourselves to radially symmetric solutions, we will use $\hat{\boldsymbol{x}} := R\hat{\boldsymbol{x}} \in B_R(\mathbf{0})$ to denote position in the original d-dimensional ball domain of radius R, whereas $\boldsymbol{x} \in B_1(\mathbf{0})$ denotes position in the normalised domain with radius 1. Solutions on the original domain shall be denoted by $\hat{\rho} \in \hat{\mathcal{L}}$ whereas equilibrium measures $\rho \in \mathcal{L}$ denote solutions on the normalised domain $B_1(\mathbf{0})$ with $\mathcal{L}$ and $\hat{\mathcal{L}}$ given in Definition 2.2. Therefore, $\text{supp}(\hat{\rho}) = B_1(\mathbf{0})$ and $\text{supp}(\rho) = B_R(\mathbf{0})$. The relationship between them is simply, $\hat{\rho}(\hat{\boldsymbol{x}}) = \hat{\rho}(R\boldsymbol{x}) = \rho(\boldsymbol{x})$.

> **Definition 2.2: Space of Particle Density Distributions**
>
> On the *full domain* $B_R(\mathbf{0}) \subset \mathbb{R}^d$, let $\hat{\mathcal{L}} := \{\rho : B_R(\mathbf{0}) \to \mathbb{R}\}$. On the *normalised domain* $B_1(\mathbf{0})$ of radius 1, let $\mathcal{L} := \{\rho : B_1(\mathbf{0}) \to \mathbb{R}\}$.

For a given density distribution ρ, we define a utility operator to help with notation, the power law potential (Definition 2.3).

> **Definition 2.3: Power Law Potential Energy**
>
> For a given equilibrium measure $\rho \in \mathcal{L}$ and $\beta \in \mathbb{R}$, the power law potential operator $U_K : \mathcal{L} \to \mathbb{R}$ is given by
>
> $$U^{(\beta)}[\rho] := \iint \|\boldsymbol{x} - \boldsymbol{y}\|_2^\beta \,\mathrm{d}\rho(\boldsymbol{x})\mathrm{d}\rho(\boldsymbol{y}) \,.$$

Note that because

$$\iint \|\boldsymbol{x} - \boldsymbol{y}\|_2^\beta \,\mathrm{d}\rho(\boldsymbol{x})\mathrm{d}\rho(\boldsymbol{y}) = \iint_{\text{supp}(\rho)^2} \|\boldsymbol{x} - \boldsymbol{y}\|_2^\beta \,\rho(\boldsymbol{x})\rho(\boldsymbol{y}) \,\mathrm{d}\boldsymbol{x}\mathrm{d}\boldsymbol{y} \,,$$

Definition 2.3 also generalises to $\hat{\rho} \in \hat{\mathcal{L}}$ thanks to the definition as a measure, and after a change of variables from $\boldsymbol{x}$ to $\hat{\boldsymbol{x}}$ and $\boldsymbol{y}$ to $\hat{\boldsymbol{y}}$, we obtain the relationship

$$U^{(\beta)}[\hat{\rho}] = R^{2d+\beta}U^{(\beta)}[\rho]\,.$$

With these preliminaries in mind, we can now formulate the problem.

> **Definition 2.4: Particle Density Distribution Problem**
>
> Given an interaction kernel $K : \mathbb{R}^+ \to \mathbb{R}$, the density distribution problem is to find the equilibrium measure $\hat{\rho} : B_R(\boldsymbol{0}) \to \mathbb{R}$ of mass $M = 1$ on a d-dimensional ball of radius $R \in \mathbb{R}^+$ that minimises the total potential $U_K[\hat{\rho}]$.

2.3   Interaction Potentials

We present a brief overview of the interaction potentials considered within the scope of this dissertation.

2.3.1   Attractive-Repulsive Potential

One example we study is that of the attractive-repulsive interaction potential, where two power law potentials compete with each other. For a given $\alpha, \beta \in \mathbb{R}\backslash\{0\}$, it is given by

$$K_{\alpha,\beta}(r) = \frac{r^\alpha}{\alpha} - \frac{r^\beta}{\beta}\,. \tag{2.5}$$

One can even consider the case when either α or β is 0 in order to arrive at a log-term (Carrillo and Huang 2017), using $\frac{x^0}{0} := \log(x)$ as a convention[2]. If the repulsive term is stronger (i.e. $\beta > \alpha$), there is no equilibrium distribution as particles simply continue repelling each other out to infinity. Attractive-repulsive potentials in general describe pairwise interactions with separate attractive and repulsive terms. In our case however, we will only refer to attractive-repulsive *power law* potentials, specifically of the form in Equation (2.5). Its equilibrium distance is at $r = 1$.

The Lennard-Jones potential ($\alpha = -12, \beta = -6$), for example, is an **intermolecular** potential, so the relevant length-scale is between molecules. Therefore, the only relevant

---

[2]Consider the Laurent series expansion of $\frac{x^a}{a} = \frac{1}{a} + \log(x) + \frac{1}{2}a\log^2(x) + \mathcal{O}(a^2)$ in the limit as $a \to 0^+$. While this limit approaches ∞ coming from the right and $-\infty$ coming from the left due to the nature of the first term in the expansion, the only remaining term in it is $\log(x)$ which is thereby chosen as a convention.

interaction is the electromagnetic force. Other forces, such as the strong force which keeps protons in the nucleus together (a force much stronger than the electromagnetic one, but effective only at much smaller distances), need not be considered at this length-scale.

2.3.2   Morse Potential

Another frequently used pairwise interaction is the *Morse potential* $K_{C_a,l_a,C_r,l_r} : \mathbb{R}^+ \to \mathbb{R}$ given by

$$K_{C_a,l_a,C_r,l_r}(r) := C_a \mathrm{e}^{-r/l_a} - C_r \mathrm{e}^{-r/l_r} \,, \tag{2.6}$$

with attractive parameters $C_a \in \mathbb{R}^+$ and $l_a \in \mathbb{R}^+$ (a 'natural length scale') and repulsive parameters $C_r, l_b \in \mathbb{R}^+$. Possible parameter ranges are given by $C_a l_a^{d-2} > 1, l_a < 1$ (D'Orsogna et al. 2006; Carrillo, Huang and Martin 2014).

2.3.3   Mixed Potential

Combining the above approaches of power law and exponential decay interaction potentials, we can define

$$K_{(C,l,\bar{a})}(r) := \frac{r^{\bar{a}}}{\bar{a}} + C e^{-r/l} \,, \tag{2.7}$$

the combination of both. Its solution via spectral methods, as introduced later in Chapters 4 and 5, can be constructed in an efficient manner exploiting the structure of the potential together with the general kernel ansatz.

2.3.4   Absolute Value Potential

As part of an exploration of the various types of kernels, one can consider

$$K_{||}(r) := |1 - r| \,, \tag{2.8}$$

as depicted in Figure 2.1. Its equilibrium distance is at $r = 1$. Because the function is not continuously differentiable, this potential is entirely un-physical but yields interesting results nonetheless (cf. Figure 3.7).

Figure 2.1: Comparing Potentials: The attractive-repulsive potential $K_{(\alpha,\beta)}(r)$ with $(\alpha, \beta) = (3.5, 1.6)$, the Morse potential $K_{(C_a,l_a,C_r,l_r)}(r)$ with $(C_a, l_a, C_r, l_r) = (1.5, 2.0, 1.0, 0.5)$, the mixed potential $K_{C,l,\overline{a}}$ with $(C, l, \overline{a}) = (1.0, 0.5, 1.8)$ and the absolute value potential $K_{||}(r)$.

The remaining chapter will briefly discuss analytical approaches taken in particle physics and computational biology to solve a version of the above problem given in Definition 2.4.

2.4   Self-Propulsion and Friction

In order to model animals in a swarm, it makes sense to consider the effect of self-propulsion (a force accelerating the particle in the direction it is already going). A set of particles with this ability are referred to as active matter - a number of individual agents within a medium. Friction is the opposite of that - a force acting against movement, cf. Equation (2.2). Self-propulsion and friction could be modelled as a quadratic of the form

$$f(\hat{v}_i) = f_{\text{self−propulsion}} - f\hat{v}_i^2 \,,$$

with $\hat{v}_i := \|\boldsymbol{\hat{v}_i}\|_2 = \left\|\frac{\mathrm{d}\boldsymbol{\hat{x}_i}}{\mathrm{d}t}\right\|_2$ the absolute value of the velocity of particle i. Running a simulation using the Morse potential given in Equation (2.6) with this friction model results in a good archetype for animal swarming behaviour, as seen in Figure 2.2. This approach is taken from D'Orsogna et al. 2006 and we are able to reproduce their simulation results.

Simulation Output with $(C_a, l_a, C_r, l_r) = (1.5, 2.0, 1.0, 0.5)$, $d = 2$

Figure 2.2: Position and velocity of $N_p = 120$ particles $d = 2$ dimensions as obtained through the molecular dynamics simulation introduced in Chapter 3. The interaction potential is a Morse potential with given parameters. Friction and self-propulsion terms are present as described in D'Orsogna et al. 2006, so using $f(v_i) = 1.6 - 0.5v_i^2$, this figure reproduces their results.

2.5   Kinetic Theory: The Vlasov Equation

A common tool in plasma physics is the Vlasov equation,

$$\frac{\partial f}{\partial t} + \frac{\mathrm{d}\boldsymbol{r}}{\mathrm{d}t} \cdot \frac{\partial f}{\partial \boldsymbol{r}} + \frac{\mathrm{d}\boldsymbol{p}}{\mathrm{d}t} \cdot \frac{\partial f}{\partial \boldsymbol{p}} = 0 \,,$$

describing the change of the phase-space distribution function $f(\boldsymbol{r}, \boldsymbol{p}, t)$ over time. The Vlasov equation is the collisionless Boltzmann equation, Vlasov replaces the collision term with long-range interactions.

An important result in kinetic theory is Liouville's theorem, stating that the total volume occupied in phase-space $\mathbb{R}^{2dN_p}$ of d coordinates for position and velocity for N_p particles is constant.

> **Theorem 2.1: Liouville's Theorem**
>
> Phase-space volume is conserved in situations of pure particle-particle interactions
>
> $$\frac{\mathrm{d}f}{\mathrm{d}t} = \frac{\partial f}{\partial t} + \sum_{i=1}^{n} \left(\frac{\partial f}{\partial q_i} \dot{q}_i + \frac{\partial f}{\partial p_i} \dot{p}_i \right) = 0 \,.$$

This observation can be used to verify, for instance, the correctness of large molecular dynamics simulations.

2.6   Swarming in Biological Settings

A 2010 paper by Cavagna et al. showed the surprising result that correlation between movement of individual starlings in bird flocks over Rome is scale-free. In contrast to the assumption that birds only mirror their neighbours' behaviour and swarming behaviour emerges as a result of that, this observation suggests that bird flocks exert collective behaviour beyond local interactions.

> "*The change in the behavioural state of one animal affects and is affected by that of all other animals in the group, no matter how large the group is.*"
> - Cavagna et al. 2010.

Their study was carried out by individually tracking each starling in the flock and using tracking algorithms to represent their 3 dimensional positions and velocities.

2.6.1   Vicsek Model

The Vicsek model (Vicsek et al. 1995) is intended for the study of active matter, in particular it is suitable to describe the swarming behaviour of large groups of animals. The fundamental idea behind the model is to assume local alignment of velocities $\boldsymbol{v_i}$ within a swarm of animals, suggesting that birds or fish imitate the direction of their neighbours. It describes how large-scale, collective motion emerges from small-scale, local interactions.

2.6.2   Long-Range Interaction Potentials

The approach we will take within the scope of this dissertation is to model animal swarms as a continuum and introduce long-range interactions where each particle not

only interacts with its closest neighbours but also far-away particles, as suggested empirically in Cavagna et al. 2010.

2.7   Analytical Solutions

Carrillo and Huang 2017 provides some analytical, radially symmetric solutions to the problem, local minima of the energy. More recently, Carrillo and Shu 2022 could show that the solution is indeed a global minimiser of the total energy. For example, with an attractive-repulsive potential as given in Equation (2.5), when $\alpha = 2$ and $\beta \in [-1, 2]$, the equilibrium measure is given by

$$\hat{\rho}(\hat{\boldsymbol{x}}) = C_\beta \cdot R^d \cdot \left(R^2 - \hat{\boldsymbol{x}}^2 \right)^{\frac{1-\beta}{2}} \,, \tag{2.9}$$

where

$$C_\beta := \frac{1}{(\beta - 1)\pi} \cos\left(\frac{(2-\beta)\pi}{2} \right) \,,$$

$$R := \left(C_\beta \cdot B\left(\frac{1}{2}, \frac{3-\beta}{2} \right) \right)^{\frac{1}{\beta-2}} \,,$$

with $B(\cdot, \cdot)$ the beta-function (cf. Definition 4.3).

<div style="text-align: right">

3

</div>

<div style="text-align: right">

Particle Simulator

</div>

While local behaviour may be according to simple rules, the aforementioned many-body systems generally exhibit complex behaviour when viewed as a whole. This behaviour can be captured in mathematical terms but also from a simulation perspective. Particle simulations such as the ones depicted in Figures 3.1 and 3.3 are well-studied in physics and scientific computing more generally. This class of simulations, in the context of intermolecular interactions, is often referred to as molecular dynamics.
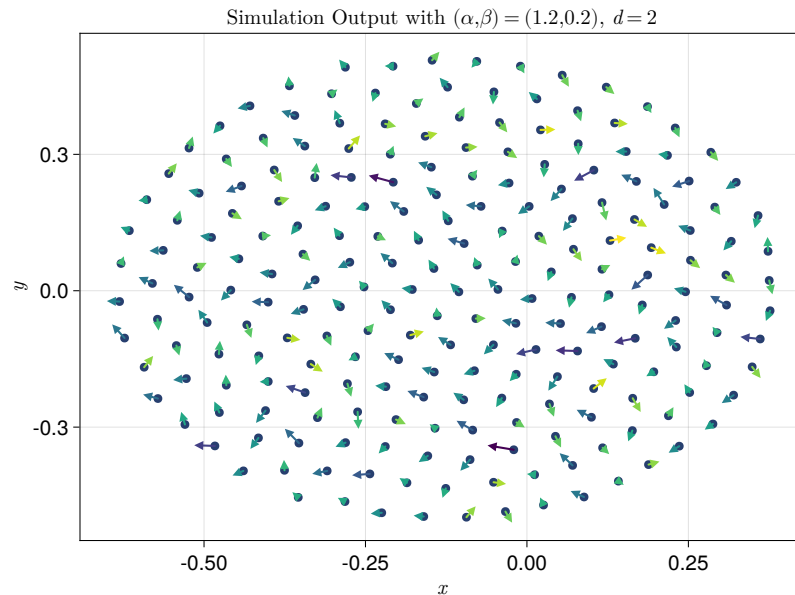

Figure 3.1: Position and velocity of particles in the simulation at a point in time. Every particle, each of equal mass m, interacts with every other particle through the interaction potential $U_{ij} = K \left(\| \boldsymbol{x_i} - \boldsymbol{x_j} \|_2 \right)$ leading to $\mathcal{O}(N_p^2)$ interactions.

Because each particle interacts with every other particle, the number of interactions scales with $\mathcal{O}(N_p^2)$, which can play a prohibitive role in terms of the computation time when increasing the number of particles $N_p \gg 1$.

Within the scope of this thesis, in order to understand the elaborate behaviour of such particle systems and also to verify results from theory and the spectral method, we provide an implementation of a simulator starting from a numerical time integrator in $\mathbb{R}^d$. In addition to the *headless* simulation software, exporting state and results for treatment by the analysis component, a Graphical User Interface (GUI) is provided to enable live insight into and interaction with the model, cf. Figure 3.2.

Figure 3.2: Screenshot of the GUI provided for the particle simulator. The top row shows the position of particles in their $[-1, 1]^d$ ($d = 2$ in this case) domain at a point t in time, the energy development over time and the current position/velocity phase space plot. Below, there are position and velocity histogram updated live along with the simulation.

The simulator can handle any number of dimensions d, even if that number must be known at compile-time so that the compiler can optimise for contiguous memory alignment which doubles the efficiency of accesses to the position and velocity arrays.

Visualisations in the GUI are restricted to two dimensions of course, but using the export feature we can visualise simulation output in $d = 3$ dimensions (cf. Figure 3.3).
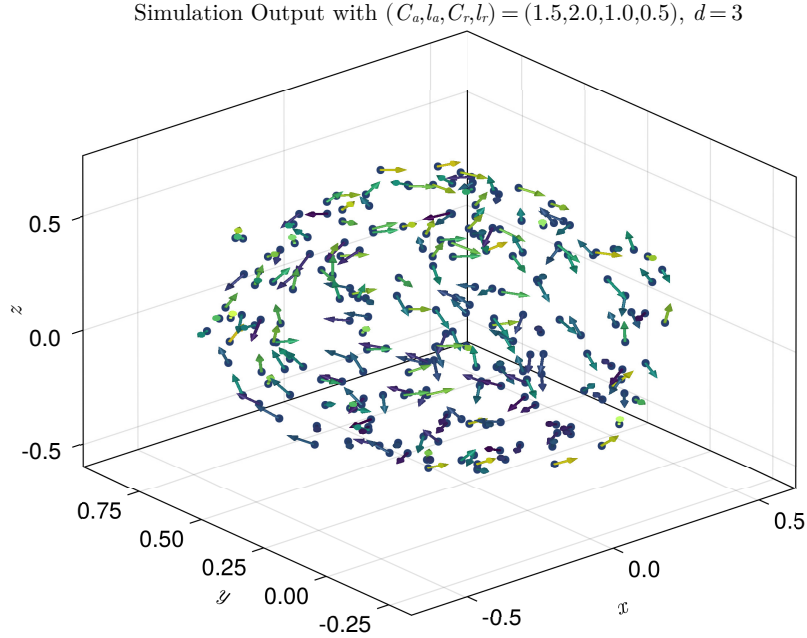

Simulation Output with $(C_a, l_a, C_r, l_r) = (1.5, 2.0, 1.0, 0.5)$, $d = 3$

Figure 3.3: Self-propelled particles in a reflective box $[-1, 1]^3$ interacting via the Morse potential $K_{C_a, l_a, C_r, l_r}(r)$ in $d = 3$ dimensions.

3.1   Available Methods

As a particular important problem in the physical sciences, there is an abundant number of simulation methods and solvers available for molecular dynamics problems.

Among them are simple forward integrators (e.g. $\boldsymbol{x_i}(t + \tau) \approx \boldsymbol{x_i}(t) + \tau \boldsymbol{v_i}(t)$ for $t > 0$ and timestep $\tau \in \mathbb{R}^+$), a generalisation of which are multistep methods. Both essentially originate from expanding the position and velocity as Taylor series in time. They work well in many general cases and error analysis is straightforward.

Named within the "Top 10 Algorithms of the 20th Century" (Cipra 2000), the Fast Multipole Method (FMM) due to Greengard and Rokhlin 1987 uses a multipole expansion of the system's Green's function to cluster together interactions with far-away particles for physical interaction potentials such as the Coulomb- or gravitational potentials. It does so by hierarchically clustering together particles based on position and treating interaction with far-away particles as a single interaction, therefore reducing the runtime from $\mathcal{O}(N_p^2)$ for each pair of particles down to $\mathcal{O}(N_p)$. FMM is

among the few methods with rigorous results available on the error. For long-range interactions however, as they are ubiquitous within this thesis (cf. the summary in Figure 2.1), the FMM is not applicable.

Another specialised method for the integration of Newton's equations of motion is Leapfrog integration, our method of choice for the C++ implementation of the N_p-body simulator.

3.1.1 Leapfrog Integration

The Leapfrog algorithm is a more effective forward integration method due to its high resistance to numerical round-off error. Except for minor changes in the way the velocity is updated, it is essentially the same as the velocity Verlet algorithm, a variant of Verlet integration with error on the order of $\mathcal{O}(\tau^4)$ with $\tau \in \mathbb{R}^+$ the timestep.

In particular, every particle i at position $\boldsymbol{x_i} \in \mathbb{R}^d$ with velocity $\boldsymbol{v_i} \in \mathbb{R}^d$ is updated using

$$\boldsymbol{x_i}(t + \tau) = \boldsymbol{x_i}(t) + \tau \cdot \boldsymbol{v_i}(t + \tau/2), \qquad \text{for } t = 0, \tau, \dots,$$
$$\boldsymbol{v_i}(t + \tau/2) = \boldsymbol{v_i}(t - \tau/2) + \tau \cdot \boldsymbol{f}[\boldsymbol{x_i}(t), t], \qquad \text{for } t = \tau, 2\tau, \dots,$$
$$\boldsymbol{v_i}(\tau/2) = \boldsymbol{v_i}(0) + \frac{\tau}{2} \cdot \boldsymbol{f}[\boldsymbol{x_i}(0), 0], \qquad \text{for } t = 0,$$

where $\boldsymbol{f_i}[\boldsymbol{x_i}(t), t] \in \mathbb{R}^d$ denotes the acceleration (sum of contributions of all forces divided by particle mass m_i). A diagram of the mechanism is given in Figure 3.4.

$$\boldsymbol{x}(0) \qquad \boldsymbol{v}(\tau/2) \qquad \boldsymbol{x}(\tau) \qquad \boldsymbol{v}(\tau + \tau/2) \qquad \boldsymbol{x}(2\tau) \quad \boldsymbol{v}(2\tau + \tau/2) \qquad \cdots$$
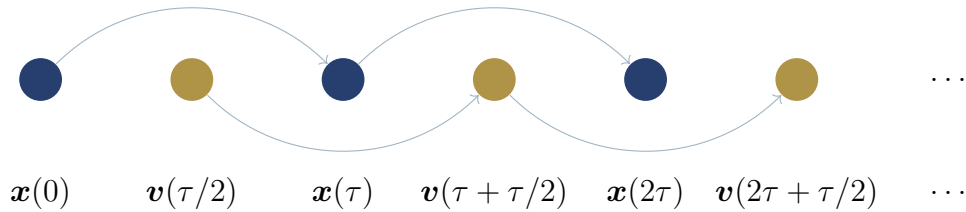
Figure 3.4: Visualisation of the Leapfrog integration method, position and velocity are updated at times shifted by $\tau/2$, half the timestep.

Verlet integration methods are a common technique in molecular dynamics for the integration of Newton's equations of motion and implemented in many solvers. Leapfrog integration can be improved to higher accuracy using Yoshida coefficients (Akita and F. Yoshida 1973). Our implementation can be found in Appendix C.

3.2   Phase Space

Each particle, at every point in time t, has a position and velocity value. In $d = 1$ dimension, one can visualise both of these quantities simultaneously in a phase space plot (cf. Figure 3.5). For $d > 1$ dimension, it is possible to either only visualise the first components $\{x_i\}_1$ and $\{v_i\}_1$ or to visualise the norm of the position (distance from the centre of mass) $r = \|x_i - x_{\text{centre}}\|_2$ and velocity $\|v_i\|_2$.
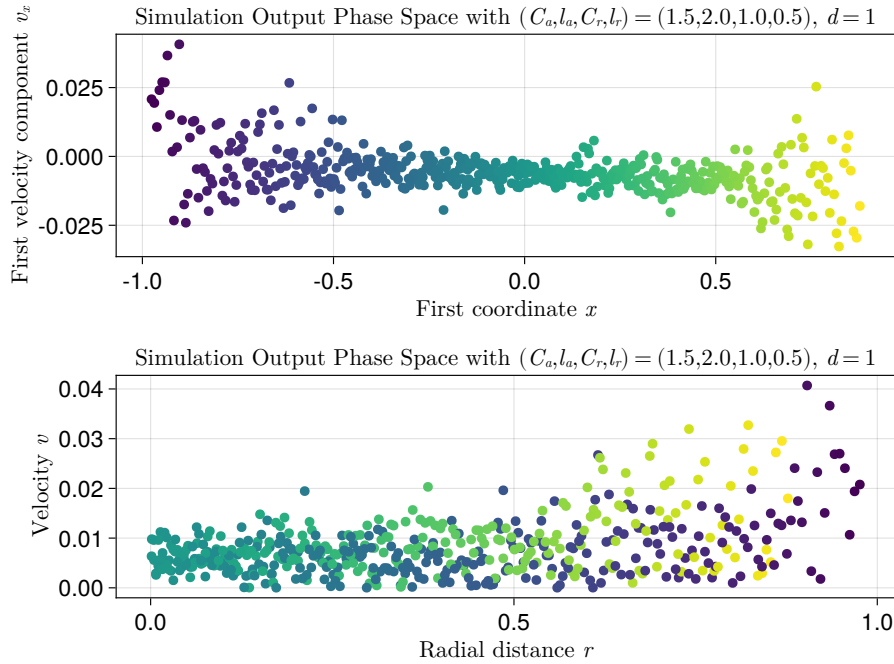

Figure 3.5: Position and velocity of $N_p = 500$ particles in a $d = 1$ simulation visualised as phase space plots using the two different visualisation mechanisms. In the top plot, one can observe natural rotation around the origin $(0,0)$ as positive velocity corresponds to movement to the right and negative velocity to leftwards movement. The colour indicates the x-coordinate of the particle, respectively (shown to visualise correspondence between the upper and the lower plot).

The behaviour of the phase space plot differs from potential to potential, most importantly one can observe multiple centers of rotation for the Morse potential in addition to the origin, whereas an attractive-repulsive potential builds up to an elliptical shape in the phase space plot.
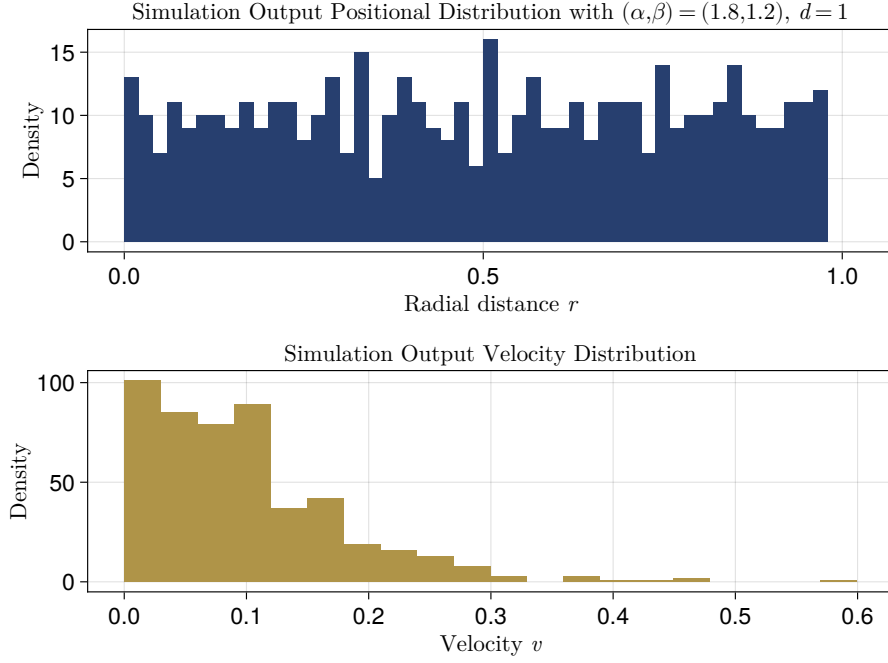
Figure 3.6: Radial Distance (r) and Velocity (v) Histograms as obtained through a long-running simulation of $N_p = 500$ particles interacting through an attractive-repulsive potential $K_{\alpha,\beta}(r)$. The spectral method introduced in Chapter 4 aims to solve for the particle density as a function of radial distance, hoping to predict the shape of the positional histogram.

In a physical setting with collision terms, the velocity distribution $f(\hat{v})$ would approach the shape of a Boltzmann distribution

$$f(\hat{v}) = \left(\frac{m}{2\pi k_B T} \right)^{\frac{3}{2}} 4\pi \hat{v}^2 \exp\left(-\frac{m\hat{v}^2}{2k_B T} \right) ,$$

with m the identical mass of each particle and velocity $\hat{v}$, k_B the Boltzmann constant and $T \in \mathbb{R}^+$ is temperature, measured in Kelvin. An exemplary velocity distribution is given in Figure 3.6.

3.3   Further Experiments

One can obtain interesting patterns using the absolute-value potential $K_{||}(r)$ as given in Equation (2.8) in $d = 3$ dimensions, cf. Figures 3.7 and 3.8. Because $K_{||}(r)$ is not continuously differentiable, the potential is not at all physical. However, due to its linear penalty (instead of exponentials or power laws) it allows for a wider range of intriguing shapes of the collection of particles.
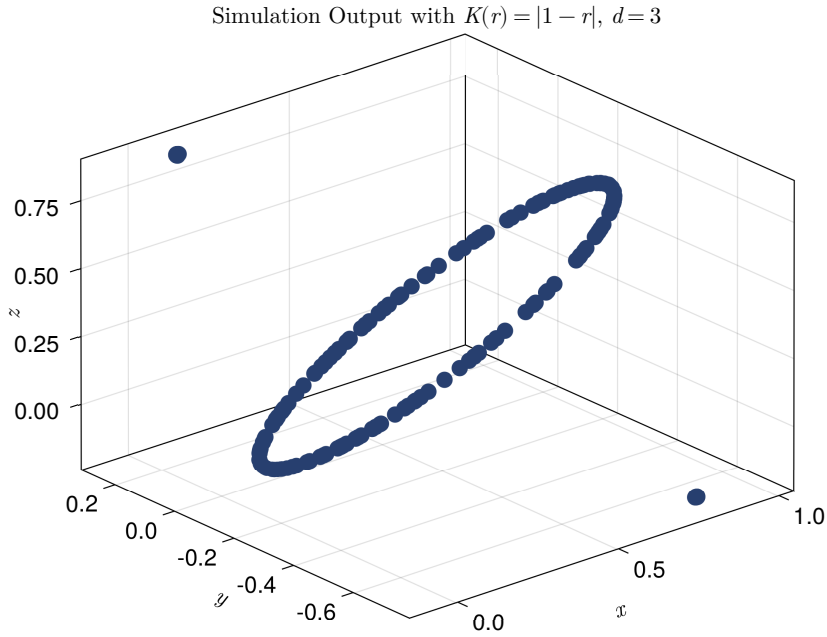

Figure 3.7: When running with $K(r) = |1 - r|$ as an interaction potential and hence, $F(r) = -\nabla K(r) = -\text{sign}(1 - r)$, in $d = 3$ dimensions a gyroscopic shape will form. The two outlying points are actually many particles above one another (high concentration of mass) and they form the axis of the rotating circle of particles.
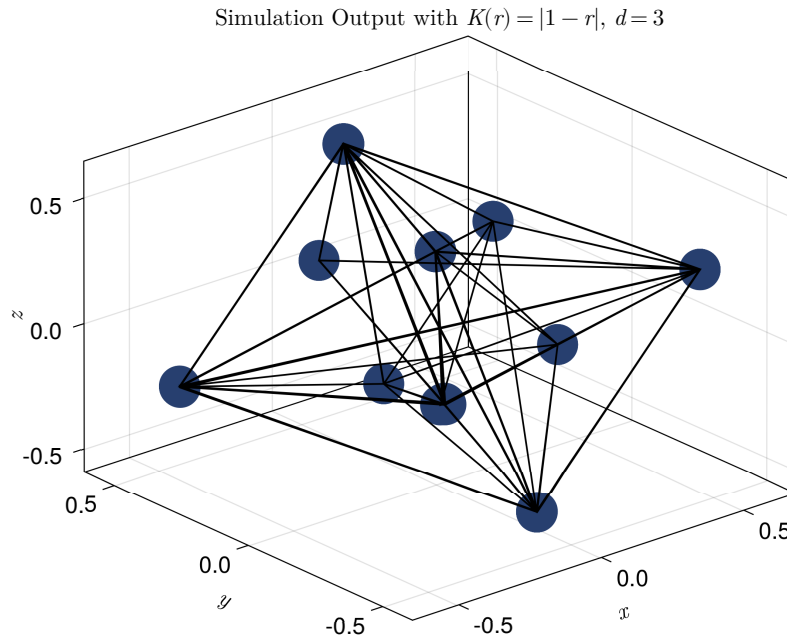
Simulation Output with $K(r) = |1 - r|$, $d = 3$

Figure 3.8: When running an $N_p = 250$ particle simulation with $K(r) = |1 - r|$ as an interaction potential in $d = 3$ dimensions the particles will align into a stable "optimal packing" arrangement. In this case, they approximate a face-centered cubic (fcc) array of spheres, potentially providing a starting point for other algorithms.

4

Spectral Method

In this chapter we will construct a spectral method in the basis of Jacobi polynomials to explore the solution of equilibrium distributions $\hat{\rho}(\hat{\boldsymbol{x}})$ based on original work in Timon S. Gutleb, Carrillo and S. Olver 2022b and Timon S. Gutleb, Carrillo and S. Olver 2022a. Starting from a many-body system and considering the continuous limit as $N_p \to \infty$, in Chapter 2 we have already established the governing equation of the particle density distribution $\hat{\rho}(\hat{\boldsymbol{x}})$ in such a system.

As mentioned in Chapter 2, the numerical approaches will be carried out on the normalised domain $B_1(\boldsymbol{0})$ and we will be looking for $\rho \in \mathcal{L}$, whilst in general we are interested in the $\hat{\rho} \in \hat{\mathcal{L}}$ solving our problem. Both versions are related by $\hat{\rho}(\hat{\boldsymbol{x}}) = \rho(\boldsymbol{x})$ and $\hat{\boldsymbol{x}} := R\boldsymbol{x}$.

Can we put together a numerical method to solve for the equilibrium distribution (cf. Definition 2.1)? Let us consider the problem from the bottom up and start from the solution: The basic idea behind spectral methods is to assume a solution $\rho(\boldsymbol{x})$ of the form

$$\rho(\boldsymbol{x}) = \sum_{k=0}^{N-1} \rho_k \varphi_k(\boldsymbol{x}), \quad \rho_k \in \mathbb{R}, \varphi_k : \mathbb{R}^d \to \mathbb{R}, \quad k = 0, ..., N-1,$$

with N coefficients $\boldsymbol{\rho} := (\rho_0, ..., \rho_{N-1})^T$ multiplying N basis functions φ_k.

4.1 Special Functions

The following section will introduce a few necessary objects and tools to understand the basis of functions we are working with to construct the spectral method, the basis of Jacobi polynomials.

We start with the Pochhammer symbol, another name for the *rising factorial*, an unusual notation for a function but standard in the context of the special functions that will be introduced on top of it.

Definition 4.1: Rising Factorial (Pochhammer Symbol)

The nth rising factorial of $x \in \mathbb{R}$ is given by

$$(x)_n := \prod_{k=0}^{n-1}(x + k) \ \in \mathbb{R} \,.$$

For example, $(3.141)_5 = 3.141 \cdot 4.141 \cdot 5.141 \cdot 6.141 \cdot 7.141$.

Remark 4.1: When the argument is a non-positive integer, the rising factorial $(-m)_n = -m \cdot (-m+1) \cdot \ldots \cdot (-m+n-1)$ vanishes when $n \geq m+1$ for $n \in \mathbb{N}$ and $m \in \mathbb{N}_0$ as 0 is among the factors.

As a second prerequisite, we introduce the closely intertwined beta- and gamma-functions (Definition 4.3, Definition 4.2).

Definition 4.2: Gamma Function

The gamma function $\Gamma : \mathbb{R}^+ \to \mathbb{R}$ is given by

$$\Gamma(x) := \int_0^\infty t^{x-1}\mathrm{e}^{-t}\mathrm{d}t \,.$$

Most importantly, for $x \in \mathbb{N}_0$, $x! = \Gamma(x+1)$.

Remark 4.2: When $x \in \mathbb{R}, n \in \mathbb{N}_0$ such that $x, x+n \notin \mathbb{Z}^-$ are not negative integers, there is an important relation to the gamma function (Definition 4.2),

$$(x)_n = \frac{\Gamma(x+n)}{\Gamma(x)} \,.$$

Definition 4.3: Beta Function

$B : \mathbb{R}^+ \times \mathbb{R}^+ \to \mathbb{R}$ is given by

$$B(x_1, x_2) := \int_0^1 t^{x_1-1}(1-t)^{x_2-1}\mathrm{d}t \,.$$

Note that following from this definition, there is a relationship with the gamma-function

$$B(x_1, x_2) = \frac{\Gamma(x_1)\Gamma(x_2)}{\Gamma(x_1 + x_2)} \, . \tag{4.1}$$

Using the Pochhammer symbol introduced in Definition 4.1, we can now define the generalised hypergeometric series $_pF_q$ (cf. Definition 4.4) and a special case of it, the Gaussian hypergeometric function (cf. Lemma 4.1).

Definition 4.4: Generalised Hypergeometric Series

The generalised hypergeometric series $_pF_q : \mathbb{R}^p \times \mathbb{R}^q \times \mathbb{C} \to \mathbb{C}$ with $p, q \in \mathbb{N}$ is given by

$$_2F_1 \begin{pmatrix} a_1, \ldots, a_p \\ b_1, \ldots, b_q \end{pmatrix} := \sum_{k=0}^{\infty} \frac{(a_1)_k \cdots (a_p)_k}{(b_1)_k \cdots (b_q)_k} \frac{z^k}{k!} \, ,$$

for $|z| < 1$ where $(\cdot)_k$ denotes the rising factorial (cf. Definition 4.1).

Note that any permutation of the first ("top") arguments $a_1, ..., a_p$ leaves the function unchanged due to commutativity of multiplication in $\mathbb{C}$. The same holds for the second ("bottom") arguments $b_1, ..., b_q$.

Lemma 4.1: Gaussian Hypergeometric Function

The $p = 2$, $q = 1$ special case of the generalised hypergeometric series can also be evaluated by

$$_2F_1 \begin{pmatrix} a_1, -n \\ b_1 \end{pmatrix} = \sum_{k=0}^{n} (-1)^k \binom{n}{k} \frac{(a_1)_k}{(b_1)_k} z^k \, ,$$

when the second argument $a_2 = -n$ is a non-positive integer, so $n \in \mathbb{N}_0$.

Proof. Starting from the definition of the generalised hypergeometric series $_pF_q$ with $p = 2$ and $q = 1$ (Definition 4.4),

$$_2F_1 \begin{pmatrix} a_1, -n \\ b_1 \end{pmatrix} = \sum_{k=0}^{\infty} \frac{(a_1)_k (-n)_k}{(b_1)_k} \frac{z^k}{k!} = \sum_{k=0}^{n} \frac{(a_1)_k (-n)_k}{(b_1)_k} \frac{z^k}{k!} \, ,$$

which can be terminated at $k = n$ due to Remark 4.1, we can express

$$\frac{(-n)_k}{k!} = \binom{-n+k-1}{k} = (-1)^k \binom{1+n-k+k-1}{k} = (-1)^k \binom{n}{k}$$

using a well-known relation between the Pochhammer symbol and the binomial coefficient (Wolfram Functions 2001; F. Olver et al. 2018) which immediately leads us

to

$$
{}_2F_1\left(\begin{array}{c} a_1, -n \\ b_1 \end{array}; z\right) = \sum_{k=0}^{n} \binom{n}{k} \frac{(a_1)_k}{(b_1)_k}(-z)^k\,,
$$

concluding the proof. □

Note that these functions are generally tricky to evaluate efficiently, only recent advancements have enabled their usage in a broader range of applications (Michel and Stoitsov 2008; Pearson, S. Olver and Porter 2017; Slevinsky 2023). Implementations are available in the HypergeometricFunctions.jl package in Julia.

More details on the Gaussian hypergeometric series, sometimes simply referred to as the hypergeometric function, its defining differential equation origin, modular interpretations and symmetries can be found in the 1997 book *Hypergeometric Functions, My Love* (M. Yoshida 1997).

4.2   Orthogonal Polynomials Forming a Basis

In order to efficiently construct a spectral method, we need an orthogonal basis.

> **Definition 4.5: Orthogonal Polynomials**
>
> Orthogonal polynomials are univariate polynomials $p_n : \mathbb{R} \to \mathbb{R}$, $p_n(x) = \sum_{k=0}^{n} c_k x^k$, $n \in \mathbb{N}_0$, that form an orthogonal basis under the inner product $\langle p_n, p_m \rangle_w$ with weight function $w(x)$, given by
>
> $$
> \langle f, g \rangle_w := \int_{D_p} f(x)g(x)w(x)\,\mathrm{d}x\,,
> $$
>
> the integral over some domain $D_p \subseteq \mathbb{R}$.

The domain of the integral, for all intents and purposes within this dissertation, will be the Chebyshev interval $D_p = [-1, 1]$.

> **Remark 4.3:** Under this inner product, multiplication by the variable x is self-adjoint, so it satisfies $\langle x \mapsto xf(x), g \rangle_w = \langle f, x \mapsto xg(x) \rangle_w$.

> **Theorem 4.1: Three-Term Recurrence Relationship**
>
> All orthogonal polynomials $\{p_0, p_1, p_2, ...\}$ (cf. Definition 4.5) have (at least) a three-term recurrence relationship of the form
>
> $$A_n p_{n+1}(x) = (B_n - x)p_n(x) + C_n p_{n-1}(x) \,.$$

Proof. For readability, let "xp_n":$= x \mapsto xp_n(x)$ denote the function resulting from multiplication of the polynomial p_n by its variable, resulting in a polynomial of $\deg(xp_n) \leq n+1$. By the linear independence of all orthogonal polynomials p_n with respect to the inner product $\langle \cdot, \cdot \rangle_w$, it must be possible to write

$$xp_n(x) = \sum_{k=0}^{n+1} \hat{a}_k p_k(x), \quad \text{for some } \hat{a}_k \in \mathbb{R}, k = 0, ..., n+1 \,.$$

Now, for all $n \geq 0$ and $m \leq n+1$ we have

$$\langle xp_n, p_m \rangle_w = \sum_{k=0}^{n+1} \hat{a}_k \langle p_k, p_m \rangle_w = \sum_{k=0}^{n+1} \hat{a}_k \delta_{i,k} = \hat{a}_m \langle p_m, p_m \rangle_w \,,$$

due to the orthogonality relationship (Theorem 4.2). Therefore,

$$\hat{a}_m = \frac{\langle xp_n, p_m \rangle_w}{\langle p_m, p_m \rangle_w} \quad \text{for all } m \leq n+1 \,. \tag{4.2}$$

But when $\underline{m < n-1}$, we have $\deg(xp_m) < n$ so $xp_m(x) = \sum_{k=0}^{n-1} \hat{b}_k p_k(x)$ for some (potentially 0) $\hat{b}_k \in \mathbb{R}$, and therefore $\langle p_n, xp_m \rangle_w = \sum_{k=0}^{n-1} \hat{b}_k \langle p_n, p_k \rangle_w = 0$, which, by the symmetry of the inner product (Remark 4.3), also implies $\langle xp_n, p_m \rangle_w = 0$ which, by Equation (4.2), allows us to conclude that the earlier coefficients $\hat{a}_m = 0$.

We recall that $xp_n(x) = \sum_{k=0}^{n+1} \hat{a}_k p_k(x)$, which in combination with our insights on the $\hat{a}_m$ above means that

$$xp_n(x) = \hat{a}_{n-1} p_{n-1}(x) + \hat{a}_n p_n(x) + \hat{a}_{n+1} p_{n+1}(x) \,,$$

concluding the proof. $\square$

For example, for the Chebyshev polynomials $T_k : [-1, 1] \to \mathbb{R}$ we have

$$T_{k+1}(x) = 2xT_k(x) - T_{k-1}(x) \,.$$

Note that the converse of Theorem 4.1 is also true, a set of polynomials of increasing degree k that has a three-term recurrence relationship is a set of orthogonal polynomials

(cf. Definition 4.5). While the original theorem is believed to be discovered by Thomas Joannes Steltjes, so before Favard 1935, to this day we still refer to it as *Favard's theorem*.

The Jacobi polynomials are then defined from $_2F_1$ as follows:

Definition 4.6: Jacobi Polynomials

Let the Jacobi polynomials $P^{(a,b)} : \mathbb{C} \to \mathbb{C}$ with $a, b \in \mathbb{R}$ be given by

$$P_n^{(a,b)}(x) := \frac{(a+1)_n}{n!} \, {}_2F_1 \left(\begin{matrix} 1 + a + b + n, -n \\ a + 1 \end{matrix} ; \frac{1-x}{2} \right),$$

where $_2F_1$ is the Gaussian hypergeometric function (Lemma 4.1) and $(\cdot)_n$ denotes the Pochhammer symbol (Definition 4.1).

Examples: Following from this definition,

$$P_0^{(a,b)}(x) = 1$$
$$P_1^{(a,b)}(x) = (a+1) + (a+b+2)\frac{x-1}{2}$$

and so on. Also note that, as with all other orthogonal polynomials, by convention indices start at 0 and therefore $\deg\left(P_k^{(a,b)}\right) = k$.

Lemma 4.2: Jacobi Polynomial Series

The Jacobi polynomials $P_n^{(a,b)}$ (Definition 4.6) can be equivalently evaluated by

$$P_n^{(a,b)}(x) = \frac{\Gamma(a+n+1)}{n! \, \Gamma(a+b+n+1)} \sum_{k=0}^{n} \binom{n}{k} \frac{\Gamma(a+b+n+k+1)}{\Gamma(a+k+1)} \left(\frac{x-1}{2}\right)^k,$$

where $\Gamma(x)$ is the gamma function (cf. Definition 4.2).

Proof. Inserting into Lemma 4.1, we have

$$\begin{aligned}
P_n^{(a,b)}(x) &= \frac{(a+1)_n}{n!} \sum_{k=0}^{n} (-1)^k \binom{n}{k} \frac{(1+a+b+n)_k}{(a+1)_k} \left(\frac{1-x}{2}\right)^k \\
&= \frac{\Gamma(a+1+n)}{n!\,\Gamma(a+1)} \sum_{k=0}^{n} \binom{n}{k} \frac{\Gamma(a+1)\Gamma(1+a+b+n+k)}{\Gamma(a+1+k)\Gamma(1+a+b+n)} \left(\frac{x-1}{2}\right)^k \\
&= \frac{\Gamma(a+1+n)}{n!\,\Gamma(1+a+b+n)} \sum_{k=0}^{n} \binom{n}{k} \frac{\Gamma(1+a+b+n+k)}{\Gamma(a+1+k)} \left(\frac{x-1}{2}\right)^k
\end{aligned}$$

using Remark 4.2. $\qquad\square$

Particularly useful properties of Jacobi polynomials for spectral methods are the explicit differentiation and three-term recurrence formulas.

Special Cases: The Gegenbauer (or ultraspherical) polynomials $C_n^{(\lambda)}$ are a special case of the Jacobi polynomials, namely when $a = b$, of which the Chebyshev polynomials of the first kind T_n are another special case of. Namely, when $a = b = -1/2$. The Chebyshev polynomials of the second kind U_n, once again regulated by a prefactor, are given by $a = b = +1/2$. In the special case when $a = b = 0$, the Jacobi polynomials reduce to the Legendre polynomials $P_n(x) = P_n^{(0,0)}(x)$, cf. F. Olver et al. 2018.

Dot-product notation: Note that in this manuscript we will use the dot-product notation between the vector of Jacobi polynomials and the coefficient vector,

$$f(x) = \sum_{k=0}^{N-1} f_k P_k^{(a,b)}(x) \quad \Leftrightarrow \quad f(x) = \boldsymbol{f} \cdot \boldsymbol{P}^{(a,b)}(x)\,,$$

to express that a function f is a linear combination of basis polynomials with coefficients $\boldsymbol{f} = (f_0, ..., f_{N-1})^T \in \mathbb{R}^N$. So $\boldsymbol{P}^{(a,b)}(x) \in \mathbb{R}^N$ is the vector of Jacobi polynomials $P_0^{(a,b)}(x)$, $P_1^{(a,b)}(x)$, ..., $P_{N-1}^{(a,b)}(x)$.

Theorem 4.2: Jacobi Polynomial Orthogonality

Jacobi polynomials $P_n^{(a,b)}(x)$ are orthogonal on $D_p = [-1, 1]$ with respect to the weight function

$$w^{(a,b)}(x) = (1 - x)^a (1 + x)^b\,,$$

so they satisfy

$$\int_{-1}^{1} (1 - x)^a (1 + x)^b P_n^{(a,b)} P_m^{(a,b)} \, \mathrm{d}x = \frac{2^{a+b+1}\Gamma(a + n + 1)\Gamma(b + n + 1)}{n!(a + b + 2n + 1)\Gamma(a + b + n + 1)} \delta_{n,m}\,,$$

with $a, b > -1$, which uniquely determines $P_n^{(a,b)}(x)$.

Proof. See, for example, Arora and Bajpai 1995.   □

As shown by, for example, "the ultraspherical method" (S. Olver and Townsend 2013), the basis of Jacobi polynomials can yield a **sparse** (i.e., only $\mathcal{O}(1)$ non-zero entries per row), and in particular, **banded** operator (all non-zero entries q_{ij} are confined to a diagonal band, so $q_{ij} = 0 \ \forall |i - j| > \tilde{b}$ for some *bandedness* $\tilde{b}$). This is due to the excellent property that derivatives of orthogonal polynomials and in particular, the

Gegenbauer (ultraspherical) polynomials, can be expressed as tridiagonal matrices acting on coefficient space.
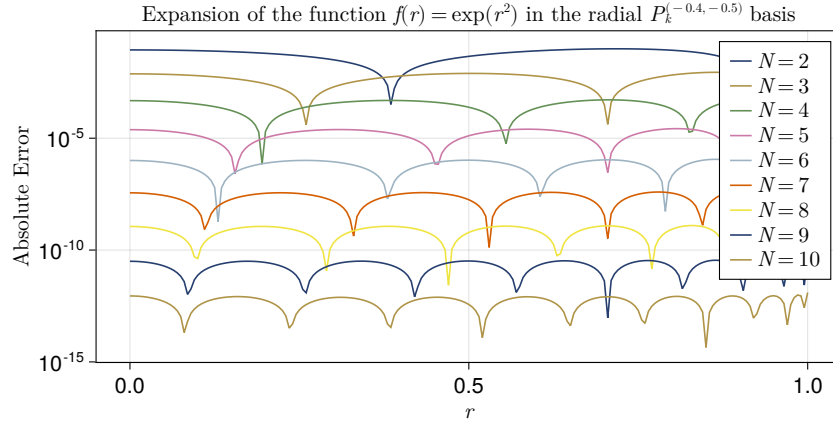

Figure 4.1: Convergence of the Jacobi polynomial expansion $f_N(x) = \sum_{k=0}^{N-1} P_k^{(a,b)}(x)$ of an example function $f(x) = \mathrm{e}^{x^2}$ with $a = -\frac{3}{4}$ and $b = -\frac{1}{2}$. Each added term improves the absolute error between the function and its expansion by a factor, so we have exponential convergence. The number of "arches" of each solution error function, occurring from the roots of $f(x) - f_N(x)$, approximately equals the order N.

An example of the approximation of a function using Jacobi polynomials is given in Figure 4.1, depicting the absolute error for expansions of growing order N.

As mentioned previously in Chapter 2, due to the absence of an external potential the solutions must be radially symmetric given that the pairwise interactions only depend on mutual distance and nothing else. So in most upcoming instances, we will work with the *radial* Jacobi polynomials, allowing us to extend the preimage of the polynomial basis from $\mathbb{R}$ to $\mathbb{R}^d$. These are simply given by $P_k^{(a,b)}\left(2\left\|\boldsymbol{x}\right\|_2^2 - 1\right)$.

Remark 4.4: The Jacobi operator is the matrix $X \in \mathbb{R}^{N \times N}$ satisfying

$$x \cdot \boldsymbol{P}^{(a,b)}(x) = \boldsymbol{P}^{(a,b)}(x) \cdot X^T.$$

The terms in the Jacobi operator are closely connected to the three-term recurrence relationship (cf. Theorem 4.1), even making the matrix tridiagonal.

4.3   Working Towards a Solution

Finally, now that we have established the basis functions, we can write down an ansatz $\rho : B_1(\mathbf{0}) \to \mathbb{R}$ for the solution of the problem, of the form

$$\rho[\boldsymbol{\rho}](\boldsymbol{x}) = \rho(\boldsymbol{x}) := \left(1 - \|\boldsymbol{x}\|_2^2\right)^{m - \frac{\alpha+d}{2}} \sum_{k=0}^{N-1} \rho_k P_k^{\left(m - \frac{\alpha+d}{2}, \frac{d-2}{2}\right)} (2 \|\boldsymbol{x}\|_2^2 - 1), \qquad (4.3)$$

with $P_k^{(a,b)}$ the Jacobi polynomials and $\{\rho_k\}_{k=0,\dots,N-1}$ the coefficients and $m \in \mathbb{N}_0$ the smallest non-negative integer such that $-d < \alpha < 2 + 2m - d$ in order to ensure that $a = m - \frac{\alpha+d}{2} > -1$ due to Theorem 4.2.

The spectral method can then be written as a linear system of the coefficients $\boldsymbol{\rho}$ as we will see in the next section. In order to establish said linear system, we first need to introduce the *inverse fractional Laplacian*, helping us with the evaluation of the power law potential integral involving radial Jacobi polynomials given in Theorem 4.3, the most important result of this chapter.

Let $(-\Delta)^{-\gamma}$ denote the inverse fractional Laplacian $\Delta := \nabla^2$ with power $\gamma \in (0, 1)$. There are numerous equivalent definitions available (cf. Kwaśnicki 2017), within the context of potential theory the Riesz potential definition (Definition 4.7) is the most common.

> **Definition 4.7: Riesz Potential**
>
> For a given function $u : \mathbb{R}^d \to \mathbb{R}$ and $\gamma \in \mathbb{R}$, its *Riesz potential* $I_\gamma[u]$ is given by
>
> $$I_\gamma[u](\boldsymbol{x}) := \frac{2^{-\gamma} \Gamma(\frac{d-\gamma}{2})}{\pi^{d/2} \Gamma(\gamma/2)} \int_{\mathbb{R}^d} \frac{u(\boldsymbol{z})}{\|\boldsymbol{x} - \boldsymbol{z}\|_2^{d-\gamma}} \mathrm{d}\boldsymbol{z} \,.$$

For $\gamma \in (0, d)$, the Riesz potential is equivalent to the inverse fractional Laplacian, so $(-\Delta)^{-\gamma} = I_\gamma$. So in the case of positive power law kernels, the equivalence to the inverse fractional Laplacian does not apply. Results on the integral will hold nevertheless and we move on to stating Theorem 4.3 from Timon S. Gutleb, Carrillo and S. Olver 2022a verbatim.

> **Theorem 4.3: Power Law Potential of the nth Jacobi Polynomial**
>
> On the d-dimensional unit ball $B_1(\mathbf{0})$ the power law potential, with power $\alpha \in (-d, 2+2m-d)$, $m \in \mathbb{N}_0$ and $\beta > -d$, of the nth weighted radial Jacobi polynomial $(1 - \|\mathbf{y}\|_2^2)^{m-\frac{\alpha+d}{2}} P_n^{\left(m-\frac{\alpha+d}{2}, \frac{d-2}{2}\right)}\left(2\|\mathbf{y}\|_2^2 - 1\right)$ reduces to a Gaussian hypergeometric function as follows:
>
> $$I_{m,n}^{\alpha,\beta}(\boldsymbol{x}) = \int_{B_1(\mathbf{0})} \|\boldsymbol{x} - \boldsymbol{y}\|_2^\beta \left(1 - \|\boldsymbol{y}\|_2^2\right)^{m-\frac{\alpha+d}{2}} P_n^{\left(m-\frac{\alpha+d}{2}, \frac{d-2}{2}\right)}\left(2\|\boldsymbol{y}\|_2^2 - 1\right) \mathrm{d}\boldsymbol{y}$$
>
> $$= \frac{\pi^{d/2}\Gamma\left(1+\frac{\beta}{2}\right)\Gamma\left(\frac{\beta+d}{2}\right)\Gamma\left(m+n-\frac{\alpha+d}{2}+1\right)}{\Gamma\left(\frac{d}{2}\right)\Gamma(n+1)\Gamma\left(\frac{\beta}{2}-n+1\right)\Gamma\left(\frac{\beta-\alpha}{2}+m+n+1\right)} {}_2F_1\left(\begin{array}{c} n-\frac{\beta}{2}, -m-n+\frac{\alpha-\beta}{2} \\ \frac{d}{2} \end{array}; \|\boldsymbol{x}\|_2^2\right).$$

Proof (adapted from Timon S. Gutleb, Carrillo and S. Olver 2022a, Section 2.5). We begin by applying Lemma 4.2 to the inside of the integrand.

$$I := \int_{B_1(\mathbf{0})} \|\boldsymbol{x} - \boldsymbol{y}\|_2^\beta \left(1 - \|\boldsymbol{y}\|_2^2\right)^a P_n^{(a,b)}\left(2\|\boldsymbol{y}\|_2^2 - 1\right) \mathrm{d}\boldsymbol{y}$$

$$= C_{a,b,n} \sum_{k=0}^n \binom{n}{k} C_{a,b,n,k} \int_{B_1(\mathbf{0})} \|\boldsymbol{x} - \boldsymbol{y}\|_2^\beta \left(1 - \|\boldsymbol{y}\|_2^2\right)^a \left(\|\boldsymbol{y}\|_2^2 - 1\right)^k \mathrm{d}\boldsymbol{y}$$

$$= C_{a,b,n} \sum_{k=0}^n \binom{n}{k} C_{a,b,n,k}(-1)^k \int_{B_1(\mathbf{0})} \|\boldsymbol{x} - \boldsymbol{y}\|_2^\beta \left(1 - \|\boldsymbol{y}\|_2^2\right)^{a+k} \mathrm{d}\boldsymbol{y}$$

where $a := m - \frac{\alpha+d}{2}$ and $b := \frac{d-2}{2}$. Note that from the first to the second line, we used $\frac{z-1}{2} = \frac{2\|\boldsymbol{y}\|_2^2 - 1 - 1}{2} = \|\boldsymbol{y}\|_2^2 - 1$.

The constants are

$$C_{a,b,n} := \frac{\Gamma(a+1+n)}{n!\Gamma(1+a+b+n)}$$

$$C_{a,b,n,k} := \frac{\Gamma(1+a+b+n+k)}{\Gamma(a+1+k)}.$$

We identify the remaining integral as the Riesz potential $I_{\beta+d}[u](\boldsymbol{x})$, cf. Definition 4.7, of the function $u(\boldsymbol{y}) := \left(1 - \|\boldsymbol{y}\|_2^2\right)^{a+k}$, which we can evaluate using Lemma 2.4 from Biler, Imbert and Karch 2011:

$$\int_{B_1(\mathbf{0})} \|\boldsymbol{x} - \boldsymbol{y}\|_2^\beta \left(1 - \|\boldsymbol{y}\|_2^2\right)^{a+k} \mathrm{d}\boldsymbol{y} = c_{\beta+d} I_{\beta+d}\left[\boldsymbol{y} \mapsto \left(1 - \|\boldsymbol{y}\|_2^2\right)^{a+k}\right](\boldsymbol{x})$$

$$= c_{\beta+d} C_{a+k,\beta,d} \cdot {}_2F_1\left(\begin{array}{c} \frac{d-(\beta+d)}{2}, -a-k-\frac{\beta+d}{2} \\ d/2 \end{array}; \|\boldsymbol{x}\|_2^2\right)$$

$$= c_{\beta+d} C_{a+k,\beta,d} \cdot {}_2F_1\left(\begin{array}{c} -\beta/2, -m-k+\frac{\alpha-\beta}{2} \\ d/2 \end{array}; \|\boldsymbol{x}\|_2^2\right),$$

as $-a - k - \frac{\beta+d}{2} = -m + \frac{\alpha+d}{2} - k - \frac{\beta+d}{2} = -m - k + \frac{\alpha-\beta}{2}$ with constants

$$c_{\beta+d} := \frac{2^{\beta+d}\pi^{d/2}\Gamma\left(\frac{\beta+d}{2}\right)}{\Gamma(-\beta/2)} \quad \text{from aforementioned definition of the Riesz potential}$$

$$C_{a+k,\beta,d} := \frac{\Gamma(a+k+1)\Gamma(-\beta/2)}{2^{\beta+d}\Gamma(d/2)\Gamma\left(a+k+\frac{\beta+d}{2}+1\right)} \quad \text{from Lemma 2.4},$$

and therefore

$$c_{\beta+d}C_{a+k,\beta,d} = \frac{2^{\beta+d}\pi^{d/2}\Gamma\left(\frac{\beta+d}{2}\right)\Gamma(a+k+1)\Gamma(-\beta/2)}{\Gamma(-\beta/2)2^{\beta+d}\Gamma(d/2)\Gamma\left(a+k+\frac{\beta+d}{2}+1\right)} = \frac{\pi^{d/2}B\left(\frac{\beta+d}{2},a+k+1\right)}{\Gamma(d/2)},$$

using Equation (4.1). So that finally,

$$\int_{B_1(\mathbf{0})} \|\boldsymbol{x} - \boldsymbol{y}\|_2^\beta \left(1 - \|\boldsymbol{y}\|_2^2\right)^{a+k} \mathrm{d}\boldsymbol{y}$$

$$= \frac{\pi^{d/2}}{\Gamma(d/2)} B\left(\frac{\beta+d}{2}, m - \frac{\alpha+d}{2} + k + 1\right) \cdot {}_2F_1\left(\begin{matrix} -\beta/2, -m - k + \frac{\alpha-\beta}{2} \\ d/2 \end{matrix}; \|\boldsymbol{x}\|_2^2\right).$$

Plugging this back into the original form above, carrying along the same parameters,

$$I = C_{a,b,n} \sum_{k=0}^{n} \binom{n}{k} C_{a,b,n,k}(-1)^k \frac{\pi^{d/2}}{\Gamma(d/2)} B\left(\cdot,\cdot\right) {}_2F_1\left(\ldots; \|\boldsymbol{x}\|_2^2\right)$$

we can apply Equation (2.1) in Timon S. Gutleb, Carrillo and S. Olver 2022a after some algebra, the special case of an identity given in Prudnikov et al. 1986 to obtain a ${}_3F_2$ (three terms in the numerator, two in the denominator) function

$$I \propto {}_3F_2\left(\begin{matrix} -\beta/2, n - \beta/2, -m - n + \frac{\alpha-\beta}{2} \\ d/2, -\beta/2 \end{matrix}; \|\boldsymbol{x}\|_2^2\right),$$

which we expand into its Definition 4.4 to see that two terms cancel:

$$I \propto \sum_{k=0}^{\infty} \frac{(-\beta/2)_k, (n - \beta/2)_k, \left(-m - n + \frac{\alpha-\beta}{2}\right)_k}{(d/2)_k(-\beta/2)_k} \frac{\|\boldsymbol{x}\|_2^{2k}}{k!},$$

which results back in a ${}_2F_1$ function (two terms in the numerator, one in the denominator), the so-called Gaussian hypergeometric function, cf. Lemma 4.1, and after combining $C_{a,b,n}$, $C_{a,b,n,k}$, $\frac{\pi^{d/2}}{\Gamma(d/2)}$ with the gamma-function expansion of $B\left(\frac{\beta+d}{2}, m - \frac{\alpha+d}{2} + k + 1\right)$ according to Equation (4.1), and cancelling terms, one finally obtains

$$I = \frac{\pi^{d/2}\Gamma\left(1+\frac{\beta}{2}\right)\Gamma\left(\frac{\beta+d}{2}\right)\Gamma\left(m+n-\frac{\alpha+d}{2}+1\right)}{\Gamma\left(\frac{d}{2}\right)\Gamma(n+1)\Gamma\left(\frac{\beta}{2}-n+1\right)\Gamma\left(\frac{\beta-\alpha}{2}+m+n+1\right)} {}_2F_1\left(\begin{matrix} n - \frac{\beta}{2}, -m - n + \frac{\alpha-\beta}{2} \\ \frac{d}{2} \end{matrix}; \|\boldsymbol{x}\|_2^2\right),$$

concluding the proof. $\square$

Lemma 2.4 from Biler, Imbert and Karch 2011; Magnus et al. 1967 is based on the *Weber-Schafheitlin* integral of two Bessel functions given in Milne-Thomson 1945. The Weber-Schafheitlin integrals are related to the fractional Laplacians of aforementioned functions because the Fourier transform of $_2F_1$ is a Bessel function. For a more generalised version of Lemma 2.4, see Huang 2014.

Also note that for even integer β, the prefactor in Theorem 4.3 sometimes contains an expression of the form $\Gamma(-n)$, $n \in \mathbb{N}$ which in principle leads to undefined behaviour (cf. Definition 4.2 together with the property that $k\Gamma(k) = \Gamma(k+1)$). However, one can consider the limit as $x \in \mathbb{R}^+$ approaches an integer n to find that

$$\lim_{x \to n} \Gamma(-x) = (-1)^{n-1}\infty \,, \quad \text{or equivalently} \quad \lim_{x \to n} \frac{1}{\Gamma(-x)} = 0 \,,$$

in which case we are lucky because $\Gamma(\beta/2 - n + 1)$ appears in the denominator of the prefactor and without any singularities in the numerator we can safely evaluate the entire expression to 0.

Because $I_{m,n}^{\alpha,\beta}(\boldsymbol{x})$ only depends on the squared radius $r^2 = \|\boldsymbol{x}\|_2^2$, let it also be denoted by $I_{m,n}^{\alpha,\beta}(r^2) = I_{m,n}^{\alpha,\beta}(\boldsymbol{x})$. Further, let

$$\overline{I}_{m,n}^{\alpha,\beta} := \frac{\left\langle x \mapsto I\left(\frac{x+1}{2}\right), P_0^{(a,b)} \right\rangle}{\left\langle P_0^{(a,b)}, P_0^{(a,b)} \right\rangle} = \frac{1}{h_0^{(a,b)}} \int_{-1}^1 I_{m,n}^{\alpha,\beta}\left(\frac{x+1}{2}\right) w^{(a,b)}(x)\, \mathrm{d}x \,, \qquad (4.4)$$

denote the 0th coefficient in a Jacobi expansion of $I_{m,n}^{\alpha,\beta}(\boldsymbol{x})$ (recall that $r^2 = \frac{x+1}{2}$ and $P_0^{(a,b)}(x) = 1$) with $h_k := \left\langle P_k^{(a,b)}, P_k^{(a,b)} \right\rangle$ the normalisation coefficients of the basis.

Adding to our collection of tools, in order to solve the problem given in Definition 2.4 we need to normalise the solution by its mass. The normalisation constant is given in Lemma 4.3, based only on a single coefficient ρ_0, allowing for a highly efficient re-normalisation.

> **Lemma 4.3: Mass of the Solution**
>
> For a given solution $\rho : B_1(\boldsymbol{0}) \to \mathbb{R}$, its *mass* $M \in \mathbb{R}$ is given by Equation (2.4). Provided the appropriate ansatz given in Equation (4.3), an expansion of weighted radial Jacobi polynomials with coefficients ρ_k, its *mass* is given by
>
> $$M[\rho[\boldsymbol{\rho}]] = \int_{\mathrm{supp}(\rho)} \rho(y)\, \mathrm{d}y = \frac{\pi^{d/2}\Gamma(a+1)}{\Gamma(a + d/2 + 1)}\, \rho_0 \,,$$
>
> so solely depending on the first coefficient ρ_0.

Proof (adapted from Timon S. Gutleb, Carrillo and S. Olver 2022a). To shorten notation, let $b = \frac{d-2}{2}$. The domain and radial symmetry of our problem suggests the use of hyperspherical coordinates:

$$
\begin{aligned}
M = \int_{B_1(\mathbf{0})} \rho(\boldsymbol{x}) \, \mathrm{d}\boldsymbol{x} &= \sum_{k=0}^{N-1} \rho_k \int_{B_1(\mathbf{0})} \left(1 - \|\boldsymbol{x}\|_2^2\right)^a P_k^{(a,b)}(2\|\boldsymbol{x}\|_2^2 - 1) \, \mathrm{d}\boldsymbol{x} \\
&= \sum_{k=0}^{N-1} \rho_k \int_{\partial B_1(\mathbf{0})} \mathrm{d}\Omega \int_{r=0}^{1} (1 - r^2)^a P_k^{(a,b)}(2r^2 - 1) r^{d-1} \, \mathrm{d}r \\
&= \Omega_d \sum_{k=0}^{N-1} \rho_k \int_{r=0}^{1} (1 - r^2)^a P_k^{(a,b)}(2r^2 - 1) r^{d-1} \, \mathrm{d}r \, ,
\end{aligned}
$$

where $\Omega_d = 2\pi^{d/2}/\Gamma(d/2)$ is the surface area of the d-dimensional hypersphere (cf. Lemma 4.4) with radius $R = 1$. Substituting $u := 2r^2 - 1$, therefore $r^2 = \frac{1+u}{2}$ and $(1 - r^2)^a = \left(\frac{1-u}{2}\right)^a = 2^{-a}(1 - u)^a$ as well as $\mathrm{d}r = \frac{\mathrm{d}u}{4r}$,

$$
\begin{aligned}
M &= 2^{-a} \Omega_d \sum_{k=0}^{N-1} \rho_k \int_{u=-1}^{1} (1 - u)^a P_k^{(a,b)}(u) r^{d-1} \frac{\mathrm{d}u}{4r} \\
&= 2^{-2} 2^{-a} \Omega_d \sum_{k=0}^{N-1} \rho_k \int_{-1}^{1} (1 - u)^a P_k^{(a,b)}(u) r^{d-2} \, \mathrm{d}u \, ,
\end{aligned}
$$

we notice that $r^{d-2} = \left(\frac{1+u}{2}\right)^{\frac{d-2}{2}} = 2^{-b}(1 + u)^b$ and so we have

$$
\begin{aligned}
M &= 2^{-2} 2^{-a} 2^{-b} \Omega_d \sum_{k=0}^{N-1} \rho_k \int_{-1}^{1} (1 - u)^a (1 + u)^b P_k^{(a,b)}(u) \, \mathrm{d}u \\
&= 2^{-(2+a+b)} \Omega_d \sum_{k=0}^{N-1} \rho_k \int_{-1}^{1} (1 - u)^a (1 + u)^b P_k^{(a,b)}(u) P_0^{(a,b)}(u) \, \mathrm{d}u \\
&= 2^{1-(2+a+b)} \frac{\pi^{d/2}}{\Gamma(d/2)} \sum_{k=0}^{N-1} \rho_k \frac{2^{a+b+1} \Gamma(a+1) \Gamma(b+1)}{0!(a+b+1)\Gamma(a+b+1)} \delta_{0,k} \\
&= \frac{\pi^{d/2} \Gamma(a+1)}{\Gamma(a+d/2+1)} \rho_0 \, ,
\end{aligned}
$$

which relies on the classical orthogonality condition of the Jacobi polynomials given in Theorem 4.2 with the 0th polynomial $P_0(u) = 1$. $\qquad \square$

Note that $M = 1$ together with $a > -1$ implies $\rho_0 > 0$ because the factor between both is positive.

> **Lemma 4.4: Surface Area of the Hypersphere**
>
> The surface area of the d-dimensional hypersphere $\partial B_R(\mathbf{0})$ is given by
>
> $$\Omega_d(R) = \frac{\mathrm{d}}{\mathrm{d}R}V_d(R) = \frac{\mathrm{d}}{\mathrm{d}R}\left(\frac{2\pi^{d/2}}{d\Gamma(d/2)}R^d\right) = \frac{2\pi^{d/2}}{\Gamma(d/2)}R^{d-1}\,.$$

Proof. We find Ω_d by evaluation of the d-dimensional Gaussian integral

$$I_d := \int_{\mathbb{R}^d} \mathrm{e}^{-\|\boldsymbol{x}\|_2^2}\,\mathrm{d}\boldsymbol{x} = \int_{\mathbb{R}}\mathrm{d}x_1...\int_{\mathbb{R}}\mathrm{d}x_d\,\mathrm{e}^{-x_1^2-\cdots-x_d^2} = \left(\int_{\mathbb{R}}\mathrm{e}^{-x_1^2}\,\mathrm{d}x_1\right)^d = (I_1)^d\,,$$

using Fubini's theorem ($I_d < \infty$). Considering the case $d = 2$, we have

$$I_2 = \int_{\mathbb{R}^2}\mathrm{e}^{-\|\boldsymbol{x}\|_2^2}\,\mathrm{d}\boldsymbol{x} = \int_0^{2\pi}\mathrm{d}\theta\int_0^{\infty}r\mathrm{e}^{-r^2}\,\mathrm{d}r = -2\pi\int_0^{-\infty}\mathrm{e}^u\frac{\mathrm{d}u}{2} = \pi\int_{-\infty}^0\mathrm{e}^u\,\mathrm{d}u = \pi\,,$$

taking the classical approach of transitioning to polar coordinates r, θ (with Jacobi determinant r^{d-1} in the d-dimensional case) immediately leading us to $I_1 = \sqrt{\pi}$. Generalising this to higher dimensions d with hyperspherical coordinates,

$$I_d = \int_{\mathbb{R}^d}\mathrm{e}^{-\|\boldsymbol{x}\|_2^2}\,\mathrm{d}\boldsymbol{x} = \Omega_d\int_0^{\infty}r^{d-1}\mathrm{e}^{-r^2}\,\mathrm{d}r = \Omega_d\int_0^{\infty}s^{d/2-1}\mathrm{e}^{-s}\frac{\mathrm{d}s}{2} = \frac{\Omega_d}{2}\Gamma(d/2)\,,$$

where once again $r := \|\boldsymbol{x}\|_2$ and using a substitution $s := r^2$, we must find equality with the above result $I_d = \pi^{d/2}$,

$$I_d = \pi^{d/2} \overset{!}{=} \frac{1}{2}\Omega_d\Gamma(d/2) \quad\Leftrightarrow\quad \Omega_d = \frac{2\pi^{d/2}}{\Gamma(d/2)}\,.$$

Now integrating over the R-ball $B_R(\mathbf{0})$, we obtain $V_d(R) := |B_R(\mathbf{0})| = \Omega_d\int_0^R r^{d-1}\,\mathrm{d}r = \frac{R^d\Omega_d}{d}$ and therefore $\Omega_d(R) = \frac{\mathrm{d}V_d(R)}{\mathrm{d}R} = \frac{2\pi^{d/2}}{\Gamma(d/2)}R^{d-1}$. $\qquad\square$

4.4   Derivation of the Operator

Similar to Definition 2.3, we can define the (single) power law operator $\mathcal{Q}^\beta$:

> **Definition 4.8: Power Law Operator $\mathcal{Q}^\beta$**
>
> The power law operator $\mathcal{Q}^\beta : \mathcal{L} \to \mathcal{L}$ is given by
>
> $$\mathcal{Q}^\beta[\rho](\boldsymbol{x}) := \int \|\boldsymbol{x} - \boldsymbol{y}\|_2^\beta\,\mathrm{d}\rho(\boldsymbol{y}) = \int_{\mathrm{supp}(\rho)} \|\boldsymbol{x} - \boldsymbol{y}\|_2^\beta\,\rho(\boldsymbol{y})\,\mathrm{d}\boldsymbol{y}\,.$$

The operator $\mathcal{Q}^\beta$ acting on an equilibrium measure $\rho(\boldsymbol{x})$ returns the energy $\tilde{E}(\boldsymbol{x}) = \mathcal{Q}^\beta[\rho](\boldsymbol{x})$ at a point $\boldsymbol{x} \in B_1(\boldsymbol{0})$ in our normalised domain.   We start by only considering a single power law operator (out of two in the case of an attractive-repulsive interaction potential $K_{\alpha,\beta}$). Substituting our ansatz given in Equation (4.3) into $\mathcal{Q}^\beta[\rho]$, we obtain

$$\mathcal{Q}^\beta[\rho](x) = \sum_{k=0}^{N-1} \rho_k \int_{B_1(\boldsymbol{0})} \|\boldsymbol{x} - \boldsymbol{y}\|_2^\beta \left(1 - \|\boldsymbol{y}\|_2^2\right)^a P_k^{(a,b)} \left(2\|\boldsymbol{y}\|_2^2 - 1\right) \mathrm{d}\boldsymbol{y}, \qquad (4.5)$$

luckily containing the integral evaluated in Theorem 4.3.

We are now interested in a numerical representation of the operator $\mathcal{Q}^\beta$ acting on the function $\rho \in \mathcal{L}$, so an equivalent (linear) operator $Q^\beta : \mathbb{R}^N \to \mathbb{R}^N$ acting on the coefficients $\rho_k \in \mathbb{R}$, $k = 0, ..., N-1$. As every finite-dimensional linear operator must have a matrix representation, we look for a $Q^\beta \in \mathbb{R}^{N \times N}$ such that

$$\mathcal{Q}^\beta[\rho](\boldsymbol{x}) = \boldsymbol{P}^{(a,b)} \left(2\|\boldsymbol{x}\|_2^2 - 1\right) \cdot Q^\beta \boldsymbol{\rho},$$

where $\boldsymbol{P}^{(a,b)} \left(2\|\boldsymbol{x}\|_2^2 - 1\right) \in \mathbb{R}^N$ is the vector of radial Jacobi polynomials $P_0^{(a,b)}(x)$, $P_1^{(a,b)}(x)$, ..., $P_{N-1}^{(a,b)}(x)$ evaluated at $2\|\boldsymbol{x}\|_2^2 - 1$ as introduced in and after Definition 4.6. Note that in the context of linear combinations of Jacobi polynomials, we will use zero-based indexing for vectors and matrices due to the convention that the first orthogonal polynomial is usually denoted by $p_0(x) = 1$, in line with $\deg(p_k) = k$.

Based on the three-term recurrence relationship (cf. Theorem 4.1), one can even determine an explicit relationship between the coefficients in the Jacobi expansion by considering the Jacobi matrix (cf. Remark 4.4). We use this recurrence relationship in our implementation to significantly speed up the construction of the operator. The recurrence coefficients used are due to Timon S. Gutleb, Carrillo and S. Olver 2022a and S. Olver, Timon Salar Gutleb et al. 2023.

Therefore, starting from Equation (4.5), we obtain

$$\mathcal{Q}^\beta[\rho](\boldsymbol{x}) = \sum_{k=0}^{N-1} \rho_k \mathcal{Q}^\beta[wP_k](\boldsymbol{x}) = \sum_{k=0}^{N-1} \rho_k \sum_{j=0}^{N-1} q_{kj}^\beta P_k^{(a,b)} \left(2\|\boldsymbol{x}\|_2^2 - 1\right)$$

$$= \sum_{j=0}^{N-1} \sum_{k=0}^{N-1} \rho_k q_{kj}^\beta P_k^{(a,b)} \left(2\|\boldsymbol{x}\|_2^2 - 1\right),$$

which we will rewrite in matrix-form,

$$\mathcal{Q}^{\beta}[\rho](\boldsymbol{x}) = \boldsymbol{P}(\boldsymbol{x}) \cdot \begin{pmatrix} \sum_{k=0}^{N-1} \rho_k q^{\beta}_{k,1} \\ \vdots \\ \sum_{k=0}^{N-1} \rho_k q^{\beta}_{k,N} \end{pmatrix} = \boldsymbol{P}(\boldsymbol{x}) \cdot \underbrace{\begin{pmatrix} q^{\beta}_{00} & \cdots & q^{\beta}_{0,N-1} \\ \vdots & \ddots & \vdots \\ q^{\beta}_{N-1,0} & \cdots & q^{\beta}_{N-1,N-1} \end{pmatrix}}_{=:Q^{\beta}} \begin{pmatrix} \rho_0 \\ \vdots \\ \rho_{N-1} \end{pmatrix}$$

$$= \boldsymbol{P}^{(a,b)}\left(2\left\|\boldsymbol{x}\right\|_2^2 - 1\right) \cdot Q^{\beta}\boldsymbol{\rho}$$

where we use $\boldsymbol{P}(\boldsymbol{x}) = \boldsymbol{P}^{(a,b)}\left(2\left\|\boldsymbol{x}\right\|_2^2 - 1\right)$ as a shorthand giving us the form of the operator matrix. Its first row, the set of coefficients for the constant Jacobi polynomial $P_0^{(a,b)}$ of each expansion of Q^{β}, weighted by the solution coefficients, adds up to the total energy E (coefficient of the constant polynomial). All remaining rows of Q^{β} contain coefficients for polynomials of degree at least 1, so their weighted contributions must add up to 0 in order for the total energy $\tilde{E}(\boldsymbol{x})$ to remain constant.

Our algorithm for the construction of Q^{β} can be found in Appendix C.

For the attractive-repulsive interaction potential $K_{\alpha,\beta}$, because each column consists of an expansion of the Jacobi polynomials, we have $q^{\beta}_{0k} = I^{\alpha,\beta}_{m,k}$.
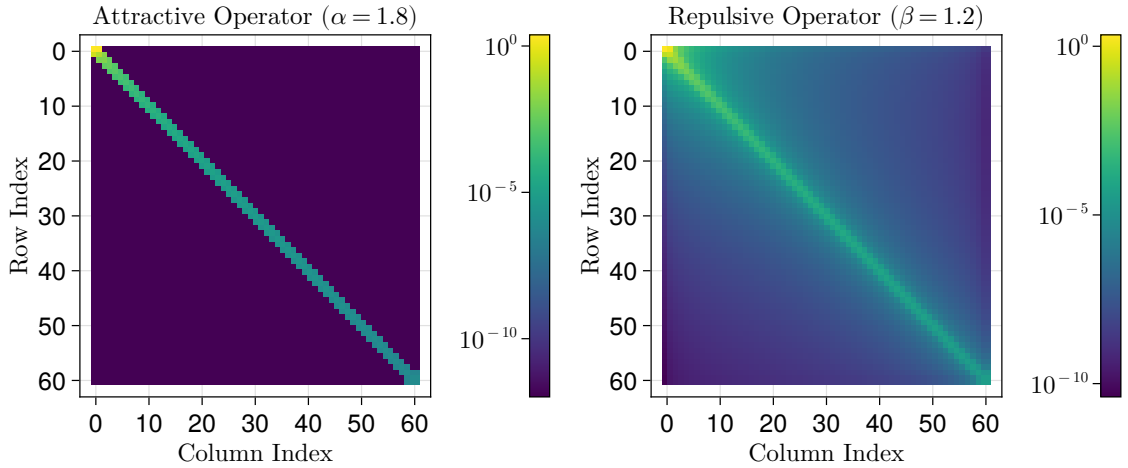
Figure 4.2: The attractive and repulsive operators (matrices) as given in Definition 4.8, the matrix values are shown in a $\log_{10}$ colour scale. Due to the choice of basis, the attractive operator is exactly banded. The repulsive parameter is only approximately banded, which the spy plots effectively demonstrate.

The exact bandedness of the attractive operator in Figure 4.2 is due to the three-term recurrence relationship of the Jacobi polynomial basis (cf. Theorem 4.1 and

Definition 4.6).   For the attractive-repulsive interaction potential $K_{\alpha,\beta}(r)$, the full operator is given by

$$
\begin{aligned}
\mathcal{Q}_{\alpha,\beta}[\hat{\rho}](\hat{\boldsymbol{x}}) &:= \int_{B_R(\mathbf{0})} K_{\alpha,\beta}\left(\|\hat{\boldsymbol{x}} - \hat{\boldsymbol{y}}\|_2\right) \hat{\rho}(\hat{\boldsymbol{y}}) \, \mathrm{d}\hat{\boldsymbol{y}} \\
&= \int_{B_R(\mathbf{0})} \left(\frac{\|\hat{\boldsymbol{x}} - \hat{\boldsymbol{y}}\|_2^{\alpha}}{\alpha} - \frac{\|\hat{\boldsymbol{x}} - \hat{\boldsymbol{y}}\|_2^{\beta}}{\beta} \right) \hat{\rho}(\hat{\boldsymbol{y}}) \, \mathrm{d}\hat{\boldsymbol{y}} \\
&= \int_{B_1(\mathbf{0})} \left(\frac{R^{\alpha} \|\boldsymbol{x} - \boldsymbol{y}\|_2^{\alpha}}{\alpha} - \frac{R^{\beta} \|\boldsymbol{x} - \boldsymbol{y}\|_2^{\beta}}{\beta} \right) \hat{\rho}(R\boldsymbol{y}) \, R^d \mathrm{d}\boldsymbol{y} \\
&= R^d \int_{B_1(\mathbf{0})} \left(\frac{R^{\alpha}}{\alpha} \|\boldsymbol{x} - \boldsymbol{y}\|_2^{\alpha} - \frac{R^{\beta}}{\beta} \|\boldsymbol{x} - \boldsymbol{y}\|_2^{\beta} \right) \rho(\boldsymbol{y}) \, \mathrm{d}\boldsymbol{y} \\
&= \frac{R^{\alpha+d}}{\alpha} \mathcal{Q}^{\alpha}[\rho](\boldsymbol{x}) - \frac{R^{\beta+d}}{\beta} \mathcal{Q}^{\beta}[\rho](\boldsymbol{x}) \,,
\end{aligned}
$$

where one needs to carefully handle the variable transform with $\mathrm{d}\hat{\boldsymbol{y}} = R^d \mathrm{d}\boldsymbol{y}$ in d dimensions whereas the vectors themselves obey $\hat{\boldsymbol{y}} = R\boldsymbol{y}$ as established previously. In matrix form that is,

$$
Q_{\alpha,\beta} := \frac{R^{\alpha+d}}{\alpha} Q^{\alpha} - \frac{R^{\beta+d}}{\beta} Q^{\beta} \,, \tag{4.6}
$$

for some interval radius $R \in \mathbb{R}^+$. The full operator for a set of example parameters is depicted in Figure 4.3. As one can see, it is approximately banded and therefore, sparse (note that the colouring is done on a log-scale).
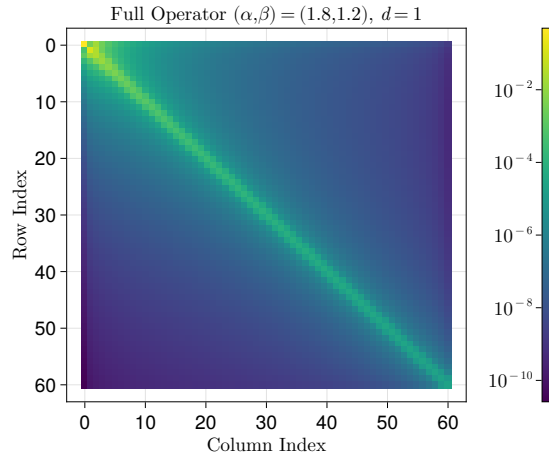
Figure 4.3: Spy plot of $Q_{\alpha,\beta}$, the combination of the attractive-repulsive operators given in Figure 4.2. Inverting this operator and applying it to $(1, 0, ..., 0)^T \in \mathbb{R}^N$ will yield the un-normalised coefficients ρ_k of the solution expansion given in Equation (4.3).

4.5   Solving a Linear System

Once the operator is computed, we are now looking for a set of solution coefficients $\boldsymbol{\rho} \in \mathbb{R}^N$ such that the total energy $E = E_{\text{kin}} + U = U = U_K[\hat{\rho}]$ (in the presence of friction, the kinetic energy will eventually dissipate, cf. Chapter 2) on the domain $D = B_R(\mathbf{0})$ is constant. That means, we are looking for $\boldsymbol{\rho} \in \mathbb{R}^N$ such that

$$\mathcal{Q}[\rho](\boldsymbol{x}) = \tilde{E}(\boldsymbol{x}) = E\,, \tag{4.7}$$

where we can expand $\tilde{E}(\boldsymbol{x}) = \boldsymbol{P}^{(a,b)}\left(2\left\|\boldsymbol{x}\right\|_2^2 - 1\right) \cdot \boldsymbol{E}$ into Jacobi polynomials with coefficients $\boldsymbol{E} = E\boldsymbol{e_1} = (E, 0, ..., 0)^T$ such that the energy is constant along the entire domain, so $\tilde{E}(\boldsymbol{x}) = E \cdot P_0^{(a,b)}\left(2\left\|\boldsymbol{x}\right\|_2^2 - 1\right) = E$. Note that because the general kernel spectral method introduced in Chapter 5 will have a different definition of the system operators, from here on, we will use $\mathcal{Q}$ and Q to denote the power law operator and its matrix representation, respectively. For the attractive-repulsive case, $\mathcal{Q} = \mathcal{Q}_{\alpha,\beta}$ and $Q = Q_{\alpha,\beta}$, respectively. In matrix form, the linear system becomes

$$Q\boldsymbol{\rho} = \boldsymbol{E} \quad \Leftrightarrow \quad \begin{pmatrix} q_{00} & \cdots & q_{0,N-1} \\ \vdots & \ddots & \vdots \\ q_{N-1,0} & \cdots & q_{N-1,N-1} \end{pmatrix} \begin{pmatrix} \rho_0 \\ \vdots \\ \rho_{N-1} \end{pmatrix} = \begin{pmatrix} E \\ \mathbf{0} \\ 0 \end{pmatrix}.$$

This equation $Q\boldsymbol{\rho} = \boldsymbol{E}$ contains two unknowns, so we need a second equation to find the full solution $\rho \in \mathcal{L}$ and, thereby, $\hat{\rho} \in \hat{\mathcal{L}}$. The second piece of information we are looking for is the mass given in Equation (2.4), which is set to $M = 1$. We start by dividing $Q\boldsymbol{\rho} = E\boldsymbol{e_1}$ by the unknown energy E,

$$Q\frac{\boldsymbol{\rho}}{E} = Q\tilde{\boldsymbol{\rho}} = \boldsymbol{e_1}\,, \tag{4.8}$$

which we can efficiently solve using readily available linear system solvers. After solving, we ensure $M\left[\rho[\tilde{\boldsymbol{\rho}}]\right] = 1$, using Lemma 4.3, leading us to our final equilibrium distribution $\rho \in \mathcal{L}$.

Hence the total potential (energy) of a given solution $\boldsymbol{\rho}$ is obtained by

$$E(R) = \{Q_{\alpha,\beta}\boldsymbol{\rho}\}_1 = \sum_{k=0}^{N-1} \rho_k \left(\frac{R^{\alpha+d}}{\alpha}\overline{I}_{m,k}^{\alpha,\alpha} - \frac{R^{\beta+d}}{\beta}\overline{I}_{m,k}^{\alpha,\beta}\right), \tag{4.9}$$

with $\overline{I}_{m,n}^{\alpha,\alpha}$ the 0th coefficient of a Jacobi polynomial expansion of $I_{m,n}^{\alpha,\alpha}(\boldsymbol{x})$ (cf. Theorem 4.3) as given in Equation (4.4).

4.5.1   Tikhonov Regularisation

For larger system sizes $N \gg 1$, numerical instability might become a concern because Fredholm equations of the first kind posed on Banach spaces, such as the one in our case, are Hilbert-Schmidt and therefore compact. That is, in the infinite case they cannot be inverted (Timon S. Gutleb, Carrillo and S. Olver 2022a). One way to address this is by regularisation of the system, which turns the first-kind into a second-kind equation.

Instead of solving the original linear system $Q\tilde{\boldsymbol{\rho}} = \boldsymbol{e_1}$, one can solve the normal system, a transformation from the original coordinates to a modified coordinate system. Left-multiplying the conjugate transpose Q^* of the matrix, it is given by

$$Q^*Q\tilde{\boldsymbol{\rho}} = Q^*\boldsymbol{e_1}\,.$$

The simplest possible Tikhonov regularisation, also referred to as Ridge regression (Hoerl and Kennard 1970), can be achieved by perturbing the normal equation by a small $s \in \mathbb{R}^+$, $s \ll 1$. The modified system therefore becomes

$$(Q^*Q + sI)\tilde{\boldsymbol{\rho}} = Q^*\boldsymbol{e_1}\,,$$

with $I \in \mathbb{R}^{N \times N}$ the identity matrix. Solving it instead of the original system given in Equation (4.8) results in a slight error in the solution, depending on the value of s, but the Tikhonov regularisation significantly improves the coefficient decay when adding more terms to the expansion. This coefficient decay is expected, after some N, further added Jacobi polynomials in the expansion should not make a significant difference, hence their coefficients should shrink for large N. The behaviour of our solver with and without regularisation is shown in Figures 4.7 and 6.3.

4.6   Results

After construction of the operator, solution through a linear system, renormalisation using the mass condition and outer optimisation of the support radius R, we finally obtain a set of solutions for arbitrary orders N, as depicted in Figure 4.4.
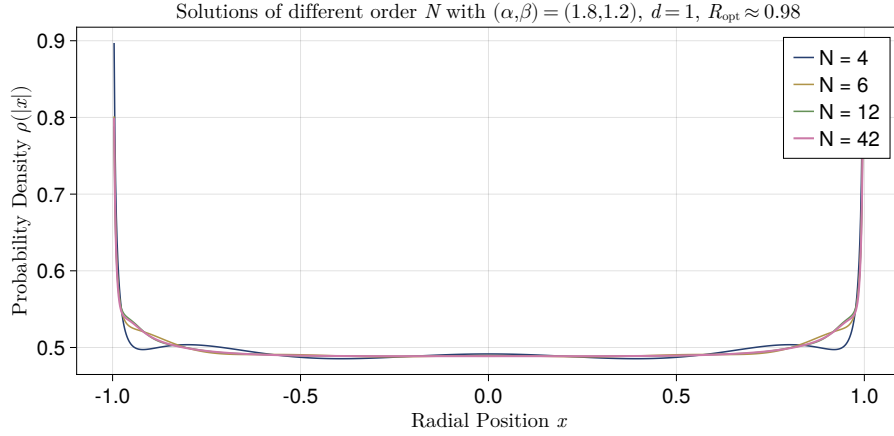
Figure 4.4: Particle density distribution function solutions ρ of increasing order N to the attractive-repulsive problem with interaction potential $K_{\alpha,\beta}(r)$, $\alpha = 2.5$ and $\beta = 1.2$. Reflected along the y-axis for better visibility of the domain.

An overview of solutions for varying parameters in an attractive-repulsive setting can be found in Figure B.3.

4.7   Outer Optimisation Routine

The unconstrained outer optimisation over the scalar value $R \in \mathbb{R}^+$, the radius of our domain $B_R(\mathbf{0})$, is carried out using Optim.jl's implementation (Mogensen et al. 2023) of the Limited-memory Broyden-Fletcher-Goldfarb-Shanno (LBFGS) optimisation method (Liu and Nocedal 1989), an extension of BFGS for low-memory usage, using an estimate for the gradient based on Automatic Differentiation (AD) techniques.

As part of a comparison between multiple optimisation approaches, LBFGS outperformed the Nelder-Mead and Newton trust region methods for our case, converging extremely quickly within only 3 iterations, 10 function calls and 10 evaluations of the gradient. While the downhill simplex method by Nelder and Mead did not converge to the desired local minimum (cf. Figure 4.5), the trust region method using Newton's method to solve a quadratic model for each subproblem (Sorensen 1982) also converged in only 3 iterations with only 4 function, gradient and Hessian evaluations. Again, the values of the gradient and Hessian (in the case of a one-dimensional optimisation, simply the first and second derivatives), are obtained using AD.

The LBFGS method converged with $\|\nabla E(R)\|_2 \approx 10^{-11}$ while the Newton trust region method converged at $\|\nabla E(R)\|_2 \approx 10^{-9}$. The entire optimisation routine with LBFGS,

including function and gradient evaluations (solving a 12×12 linear system), takes (28 ± 4) ms on an Intel® i7-5600U CPU running at 2.6 GHz.
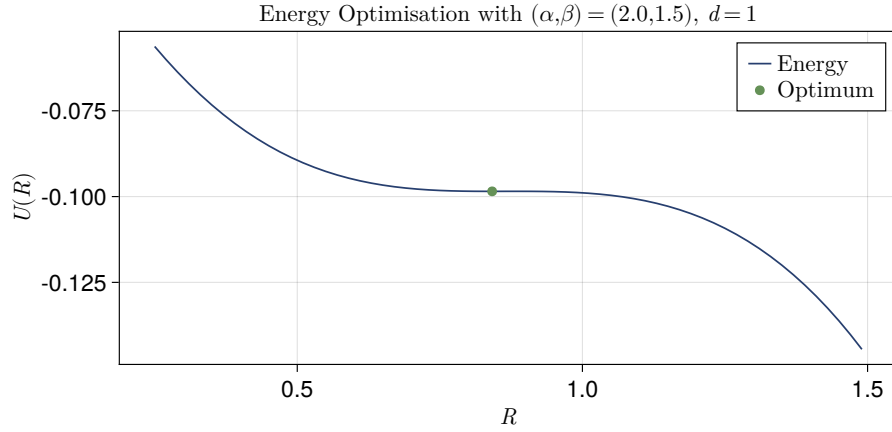
Figure 4.5: The total potential U as a function of the support radius R. This is the goal function minimised by the outer optimisation routine.

Note that using this setup, the operators themselves do not need to be recomputed upon a change in R, cf. Equation (4.6). The provided implementation uses Least Recently Used (LRU) caching to automatically store operators for a given parameter set and order N.

Lemma 4.5: Unique Energy Minimum

Assuming an $N = 1$ expansion of the density distribution ρ according to Equation (4.3) with $m \in \mathbb{N}_0$, for a feasible attractive-repulsive interaction potential $K_{\alpha,\beta}(r) = \frac{r^\alpha}{\alpha} - \frac{r^\beta}{\beta}$ with $\alpha > \beta$ and $\alpha > 0$, the energy minimum $E_{\min} = E(R_{\mathrm{opt}})$ is unique and given by

$$R_{\mathrm{opt}} = \left(\frac{\alpha(\beta + d)\overline{I}^{\alpha,\beta}_{m,0}}{\beta(\alpha + d)\overline{I}^{\alpha,\alpha}_{m,0}} \right)^{\frac{1}{\alpha - \beta}},$$

with $\overline{I}^{\alpha,\alpha}_{m,n}$ as given in Equation (4.4).

Proof. Starting from the total energy given in Equation (4.9), we obtain the first derivative as

$$\frac{\partial E}{\partial R} = \frac{\partial}{\partial R} \rho_0 \left(\frac{R^{\alpha+d}}{\alpha} \overline{I}^{\alpha,\alpha}_{m,k} - \frac{R^{\beta+d}}{\beta} \overline{I}^{\alpha,\beta}_{m,k} \right) = \rho_0 \frac{\alpha + d}{\alpha} R^{\alpha+d-1} \overline{I}^{\alpha,\alpha}_{m,k} - \rho_0 \frac{\beta + d}{\beta} R^{\beta+d-1} \overline{I}^{\alpha,\beta}_{m,k},$$

as $\frac{\partial \rho_0}{\partial R} = 0$ for $N = 1$. Setting the derivative to 0 to find the extremata,

$$\frac{\partial E}{\partial R} = 0 \quad \Leftrightarrow \quad \frac{\alpha + d}{\alpha} R^\alpha \overline{I}_{m,k}^{\alpha,\alpha} = \frac{\beta + d}{\beta} R^\beta \overline{I}_{m,k}^{\alpha,\beta} \quad \Leftrightarrow \quad R^{\alpha - \beta} = \frac{\alpha(\beta + d)}{\beta(\alpha + d)} \frac{\overline{I}_{m,k}^{\alpha,\beta}}{\overline{I}_{m,k}^{\alpha,\alpha}},$$

we obtain a unique extremum $R_{\text{opt}} := \left(\frac{\alpha(\beta+d)\overline{I}_{m,0}^{\alpha,\beta}}{\beta(\alpha+d)\overline{I}_{m,0}^{\alpha,\alpha}} \right)^{\frac{1}{\alpha - \beta}}$. Because we must have $\alpha > \beta$ for any stable solution, $\lim_{r \to \infty} K_{\alpha,\beta}(r) = \infty$ and more importantly,

$$\lim_{R \to \infty} E(R) = \lim_{R \to \infty} \rho_0 R^d \left(\frac{R^\alpha}{\alpha} \overline{I}_{m,k}^{\alpha,\alpha} - \frac{R^\beta}{\beta} \overline{I}_{m,k}^{\alpha,\beta} \right) = \infty \,,$$

since both $\overline{I}_{m,k}^{\alpha,\alpha}, \overline{I}_{m,k}^{\alpha,\beta} < \infty$, $\alpha > 0$ and $M > 0 \Rightarrow \rho_0 > 0$, indicating that any $R_{\text{opt}} > 0$ must be a minimum between the endpoints $R = 0$ and $R = \infty$. $\square$

There is strong numerical evidence that the energy minimum is also unique for $N > 1$. Despite significant effort, this remains difficult to prove [1]. Even for $N = 2$, attempting a direct substitution of $\boldsymbol{\rho}$ through the explicit inversion of a 2×2 matrix, leads to finding the roots of a quintic polynomial for which it is well-known that no explicit formula exists.

While the exact value of R_{opt} in Lemma 4.5 is not helpful for higher expansion orders as it only holds for $N = 1$, it provides a reliable initial guess for the optimisation routine. Further, $R_{\text{opt}} > 0$ is an approximate (necessary) condition for the existence of an energy minimum of a given combination of α and β.

4.8   Comparison with Analytic Solutions

As introduced in Section 2.7, there are some analytical solutions available which allow us to perform further analysis of the numerical method in these special cases.

The major advantage of a spectral method is its so-called *spectral convergence*, sometimes also referred to as exponential convergence, cf. Definition 4.9 from Schönlieb 2015, verbatim.

> **Definition 4.9: Spectral Convergence**
>
> An N-point approximation φ_N of a function f converges to f at spectral speed if $|\varphi_N - f|$ decays pointwise in $[-1, 1]$ faster than $\mathcal{O}(N^{-p})$ for any $p = 1, 2, \ldots$ so $p \in \mathbb{N}$.

---

[1]Naming "numerical evidence" is a current topic of discussion in the numerical analysis community

For a given set of parameters with a known analytical solution (cf. Section 2.7), we compare growing orders of the spectral method's solution with thanalyticalic expression in a set of 200 points and plot the pointwise error, cf. Figure 4.6. The figure also shows how the outer optimisation routine approaches the optimal R_{opt} closer and closer for growing orders N.
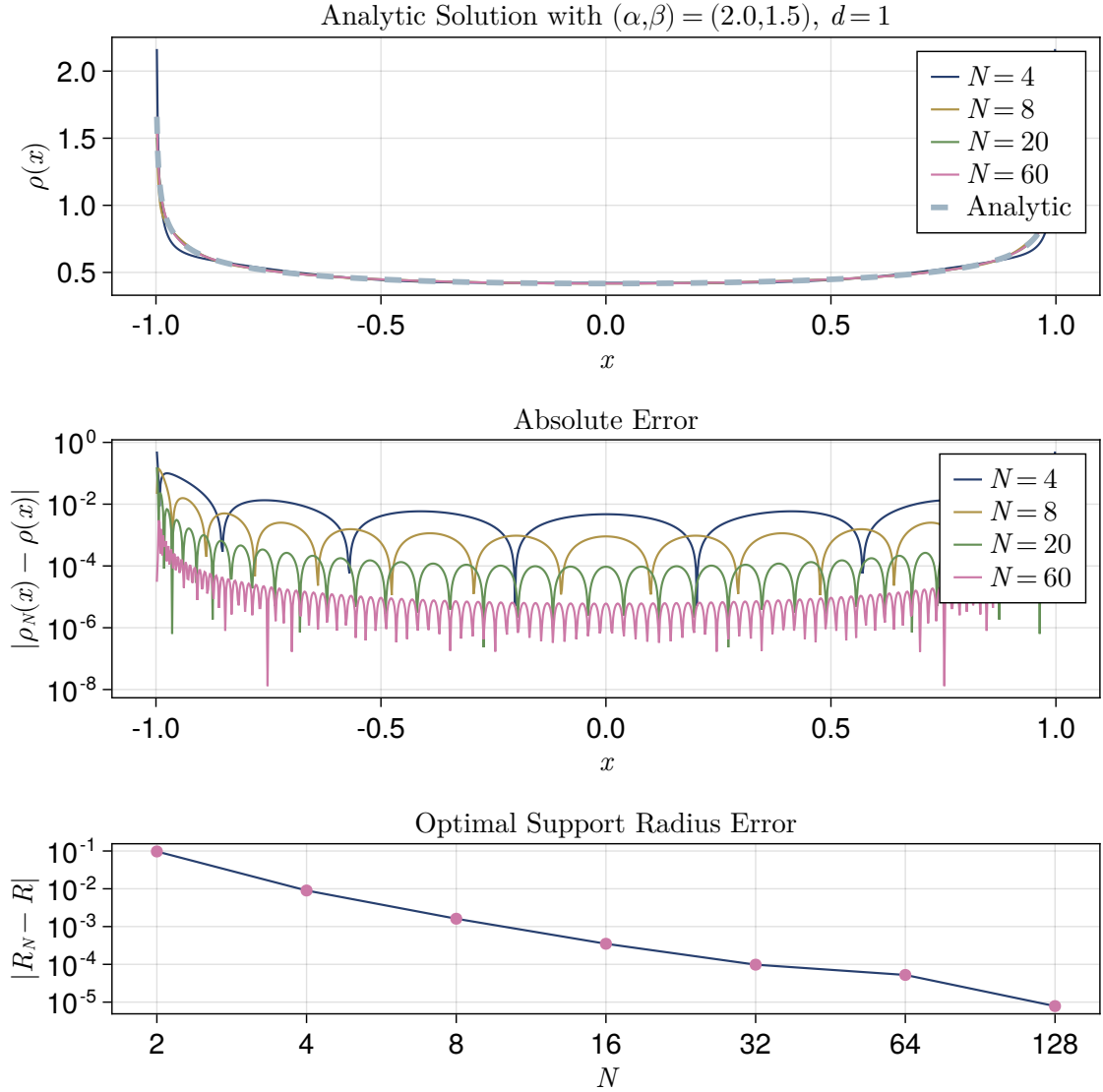
Figure 4.6: The analytical solution $\rho(x)$ given in Equation (2.9) compared to the (spectral method) solutions of different order N. The "arches" occur as a result of the roots of $\rho(x) - \rho_N(x)$, their number approximately equals the order N (a polynomial of degree N has at most N roots).

When choosing a specific parameter $a = \frac{1-\beta}{2}$, due to the choice of weighted basis in Equation (4.3), as compared to the form of the analytical solution in Equation (2.9), convergence will be immediate after only one coefficient ($N = 1$). While this is excellent convergence behaviour, it is not very interesting for convergence analysis. For this reason, we set $a = m - \frac{\alpha+d}{2}$ in the usual way and obtain convergence results in Figure 4.7. There are more analytical solutions available for other parameter ranges, which we will not analyse within the scope of this dissertation.
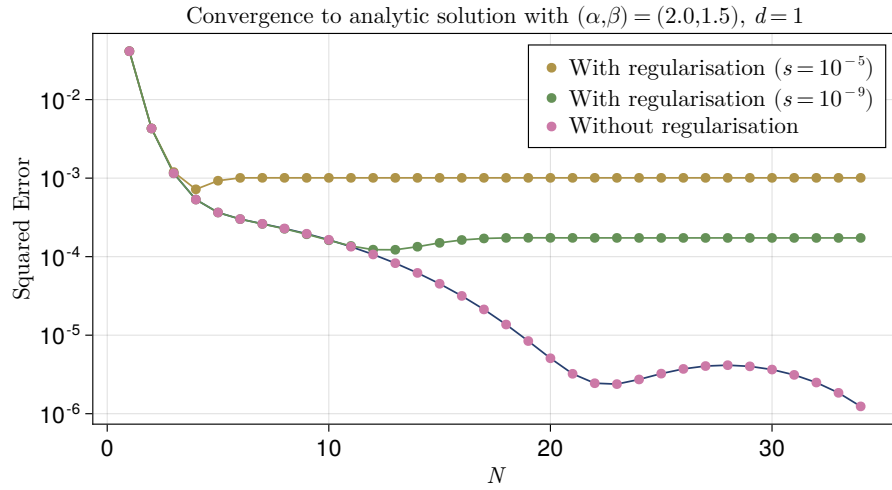
Figure 4.7: Convergence of the numerical solution to the knowanalyticalic solution (cf. Equation (2.9)) in a special case where it is known, squared error plotted as a function of the highest order in the expansion N. With Tikhonov regularisation, the accuracy is restrained to a

4.9 Discussion

For unknown analytical solutions, one can still perform a "step-by-step" convergence analysis, comparing the difference between two solutions of adjacent order for growing order N. This does not always lead to clean improvements for every N, as can be seen in Figure 4.8.
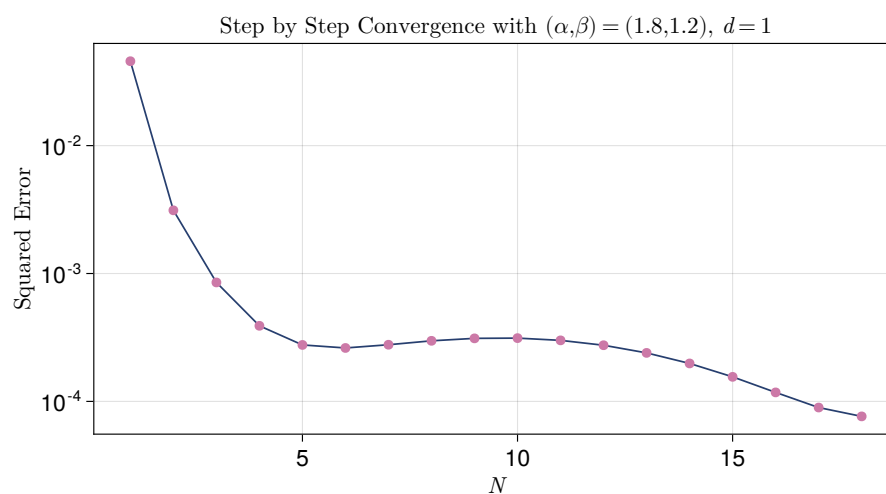
Figure 4.8: Step-by-step convergence of numerical solutions $\rho_N(x)$ as compared to $\rho_{24}(x)$, visualised using the squared error of the pointwise evaluation of both functions in 200 points.

<div style="text-align: right; font-size: 3em;">5</div>

General Kernel Spectral Method

Now that we know how to treat power law potentials in the construction of a spectral method for the solution of equilibrium measures, can we consider more general kernels as well? The approach in this chapter is to expand a general kernel K in a power law basis and utilise the methodology introduced in the previous chapter to construct a general kernel spectral method.

5.1 Expansion of the General Kernel

More specifically, one choice of basis that could be made is the basis of monomials (so integer powers of the power law kernel basis). Using standard methods from function approximation theory, we expand the general kernel $K : \mathbb{R}^+ \to \mathbb{R}$ in the basis of G Jacobi polynomials (cf. Definition 4.6)

$$K(r) \approx \sum_{l=0}^{G-1} \tilde{g}_l P_l^{(a,b)} \left(2r^2 - 1\right) , \quad \tilde{\boldsymbol{g}} := (\tilde{g}_0, ..., \tilde{g}_{G-1})^T \in \mathbb{R}^G ,$$

which we then reproject into the monomial basis to obtain the monomial coefficients $g_l \in \mathbb{R}$ such that

$$K_G(r) = \sum_{l=0}^{G-1} g_l r^l \approx K(r) , \quad \boldsymbol{g} := (g_0, ..., g_{G-1})^T \in \mathbb{R}^G . \tag{5.1}$$

For versatility in the choice of basis, we obtain the monomial coefficients of a given kernel $K(r)$ by $\boldsymbol{g} = B\tilde{\boldsymbol{g}}$, where $B \in \mathbb{R}^{G \times G}$ is the conversion matrix between the basis of radial Jacobi polynomials and the basis of monomials. The basis conversion matrix B is easily obtained by projection of each monomial into the Jacobi basis, more specifically the kth column ($k \in \mathbb{N}_0$) is comprised of the Jacobi coefficients of r^k.

5.2   Description of the Method

Given the ansatz in Equation (4.3), the total energy of the equilibrium measure (cf. Definition 2.1) is given by

$$U_{K_G}[\hat\rho] = \iint K_G\left(\|\hat{\boldsymbol{x}} - \hat{\boldsymbol{y}}\|_2\right) \mathrm{d}\hat\rho(\hat{\boldsymbol{x}})\mathrm{d}\hat\rho(\hat{\boldsymbol{y}}) = \sum_{l=0}^{G-1} g_l \iint \|\hat{\boldsymbol{x}} - \hat{\boldsymbol{y}}\|_2^l \,\mathrm{d}\hat\rho(\hat{\boldsymbol{x}})\mathrm{d}\hat\rho(\hat{\boldsymbol{y}})$$

$$= R^{2d} \sum_{l=0}^{G-1} g_l R^l \iint \|\boldsymbol{x} - \boldsymbol{y}\|_2^l \,\mathrm{d}\rho(\boldsymbol{x})\mathrm{d}\rho(\boldsymbol{y}) = R^{2d} \sum_{l=0}^{G-1} g_l R^l U^{(l)}[\rho]\,,$$

using Definition 2.3. The *general kernel operator* $\mathcal{Q}_G : \mathcal{L} \to \mathcal{L}$, analogous to $\mathcal{Q}_{\alpha,\beta}$ for the attractive-repulsive case, is given by

$$\mathcal{Q}_G[\hat\rho](\hat{\boldsymbol{x}}) := \int_{B_R(\boldsymbol{0})} K_G\left(\|\hat{\boldsymbol{x}} - \hat{\boldsymbol{y}}\|_2\right) \hat\rho(\hat{\boldsymbol{y}}) \,\mathrm{d}\hat{\boldsymbol{y}} = \int_{B_R(\boldsymbol{0})} \sum_{l=0}^{G-1} g_l \|\hat{\boldsymbol{x}} - \hat{\boldsymbol{y}}\|_2^l \,\hat\rho(\hat{\boldsymbol{y}}) \,\mathrm{d}\hat{\boldsymbol{y}}$$

$$= \sum_{l=0}^{G-1} g_l R^{l+d} \int_{B_1(\boldsymbol{0})} R^l \|\boldsymbol{x} - \boldsymbol{y}\|_2^l \,\rho(\boldsymbol{y}) \,\mathrm{d}\boldsymbol{y} = \sum_{l=0}^{G-1} g_l R^{l+d} \mathcal{Q}^l[\rho](\boldsymbol{x})\,,$$

where $\mathcal{Q}^l \in \mathbb{R}^{N \times N}$ is the power law operator (cf. Definition 4.8). Its matrix representation Q_G acting on coefficient space is derived analogously from $Q^\beta \in \mathbb{R}^{N \times N}$.

The solution process then follows analogously from Chapter 4. A spy plot of the full operator may be found in Figure 5.1, resulting solutions in Figure 5.2.

Choice of the Jacobi Basis: As for the attractive-repulsive case, the radial Jacobi basis $P_k^{(a,b)}\left(2\|\boldsymbol{x}\|_2^2 - 1\right)$ requires two parameters $a, b > -1$ (cf. Definition 4.6 and Theorem 4.2). In the attractive-repulsive case, these are chosen based on α, some $m \in N_0$ and the dimension d. Our method chooses the most dominant monomial power in the expansion ($l_{\mathrm{dom}} = \max_{l \in \{0,\dots,G-1\}} |g_l|$) in place of α to obtain $a = m - \frac{l_{\mathrm{dom}}+d}{2}$. This choice once again places a restriction on either $l_{\mathrm{dom}} < G$ and therefore G, or on the parameter $m \in \mathbb{N}_0$. That is, $-d < l_{\mathrm{dom}} < 2 + 2m - d$. This is to ensure that the most dominant contribution to the operator is exactly banded (as established in Section 4.4), making the full operator Q_G as diagonally dominant as possible. The second parameter remains $b = \frac{d-2}{2}$.
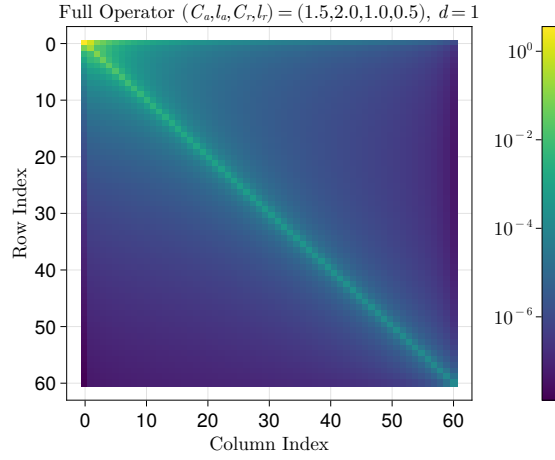
Figure 5.1: The full operator constructed from the $G = 8$th order monomial expansion K_G of the Morse potential function $K_{C_a,l_a,C_r,l_r}(r)$ with parameters as given above.

Solutions for the Morse potential can be found in Figure 5.2 for varying order N, solutions for varying order G (the number of terms in the polynomial expansion of the kernel $K(r)$) are depicted in Figure 5.3.
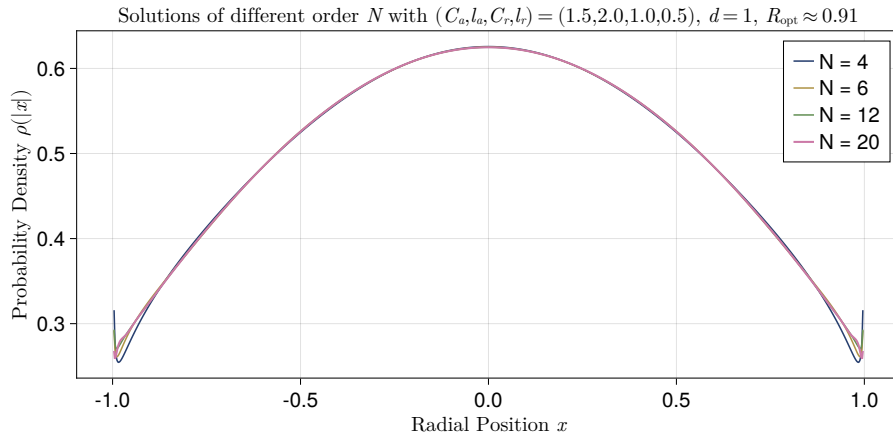
Figure 5.2: Solutions $\rho_N(x)$ of increasing order N in the general kernel setting with a monomial expansion of highest order $G = 8$ of the Morse potential $K_{C_a,l_a,C_r,l_r}(r)$.

Instead of increasing the order of the expansion in the solution ansatz (cf. Equation (4.3)), one can increase the expansion order of the general kernel, G to ensure a good match between the general kernel expansion and $K_G(r)$.

General Kernel Solution with G Monomial Terms $(C_a,l_a,C_r,l_r)=(1.5,2.0,1.0,0.5)$, $d=1$, $R_{\text{opt}} \approx 0.9$
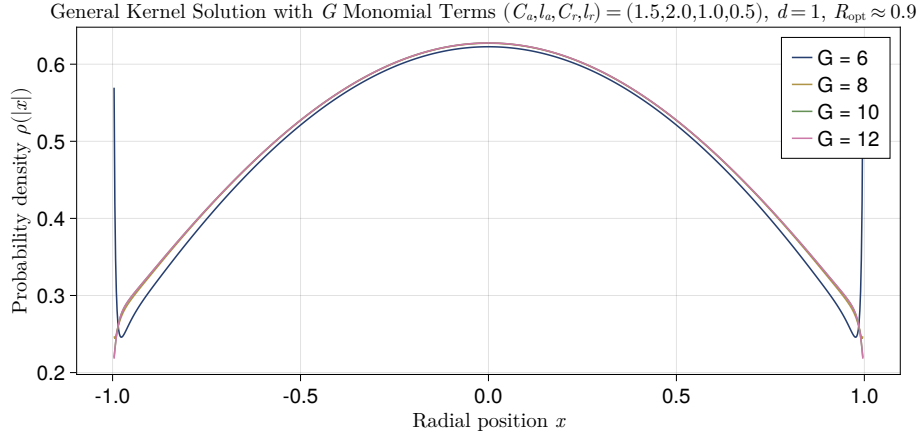
Figure 5.3: Solutions $\rho_8(x)$ for an increasing number of terms G in the mono-mial expansion of a general kernel K, in this case given by the Morse potential $K_{C_a,l_a,C_r,l_r}(r)$. So each solution $\rho_8(x)$ is a linear combination of 8 Jacobi polyno-mials together with a weight, cf. Equation (4.3). The singularities of lower order solutions disappear for higher G, which extensive simulation results attest.

As one can see, the solutions improve the better the approximation of the general kernel K becomes with growing order G of its monomial expansion. Figure 5.4 illustrates this behaviour by showing the rapid improvement of the squared error for growing order G.
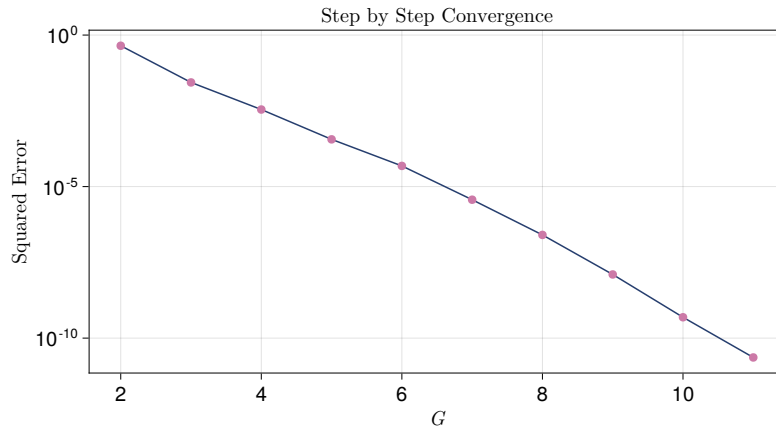
Figure 5.4: Convergence of numerical solutions $\rho_N(x)$ as compared to $\rho_{24}(x)$, visualised using the squared error of the pointwise evaluation of both functions in 200 points. The solver again uses $K(r) = K_{C_a,l_a,C_r,l_r}(r)$.

Solutions for varying support radius R can be found in Figure 5.5.
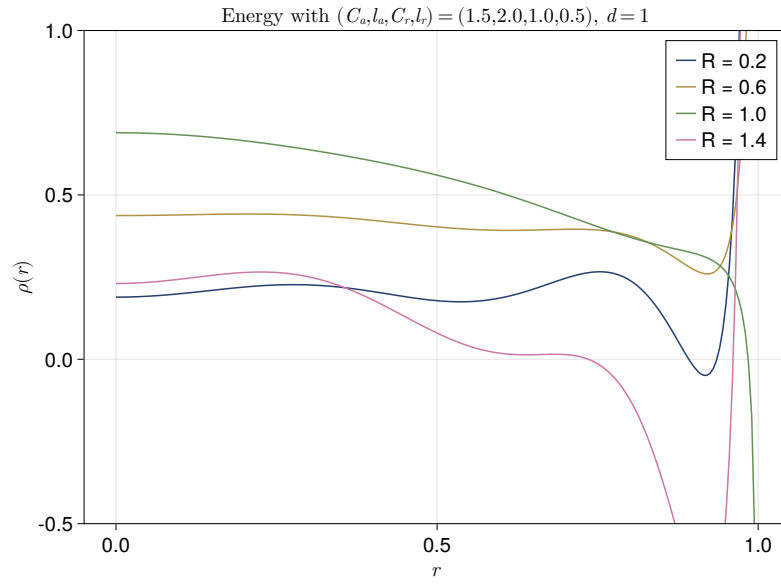
Figure 5.5: General kernel solutions ($N = 6$, $G = 8$) with varying R when using the Morse potential $K_{C_a,l_a,C_r,l_r}(r)$ with parameters as given above.

6

Implementation and Results

Simulating and solving for the same parameters, we can compare the radial distribution histogram of the simulation output with the obtained, radially symmetric, equilibrium distribution $\rho \in \mathcal{L}$, cf. Figure 6.1.

Particle Simulation Output Distribution with $(C_a, l_a, C_r, l_r) = (1.5, 2.0, 1.0, 0.5)$, $d = 1$
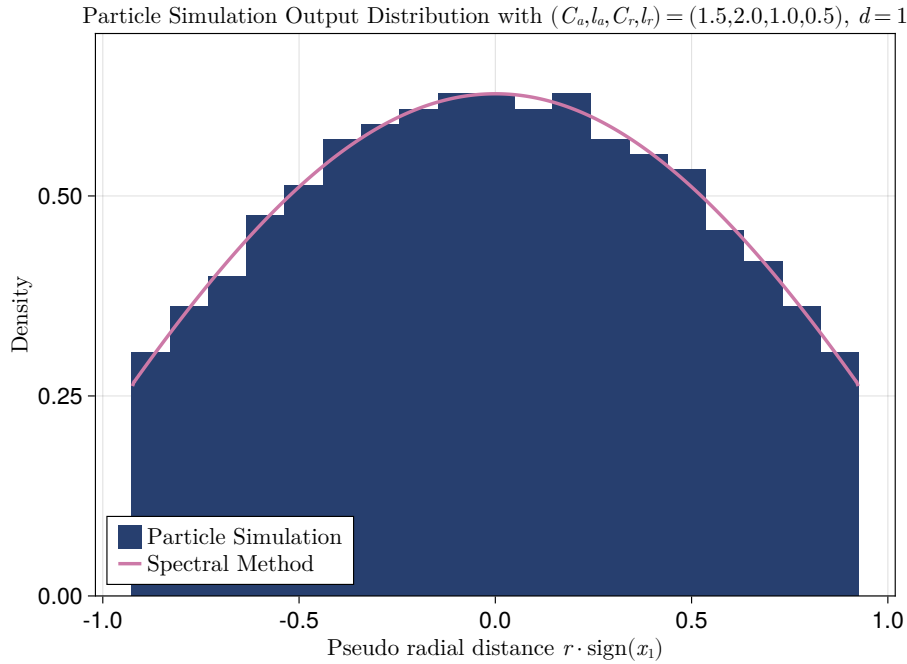
Figure 6.1: Comparison of the radial distance histogram from the simulation output with the $G = 8$ general kernel solver's equilibrium measure $\rho_{12}(r)$ at R given by the simulator, so without using the outer optimisation routine. The interaction potential in this example is $K(r) = K_{C_a, l_a, C_r, l_r}(r)$ with parameters given above.

6.1   Further Discussion

6.1.1   Well-Conditionedness

A common flaw of spectral (collocation) methods, one could think of them as the highest-order limit of finite difference schemes, is their problematic conditioning behaviour, often caused by to the ill-conditioning of spectral differentiation matrices (Trefethen 2019).

Ideally, we would like the condition number $\kappa_2(Q) \in \mathbb{R}$ to be independent of the order N to which we solve our problem. For well-conditionedness of the operator, we need

$$\kappa_2(Q) := \frac{\sigma_{\max}(Q)}{\sigma_{\min}(Q)} = \frac{\|Q\|_2}{\|Q^{-1}\|_2} = \mathcal{O}(1)$$

and not $\mathcal{O}(N)$ or even higher orders. The poor conditioning behaviour of the operators in the attractive-repulsive case can be seen in Figure 6.2. Attempts at using a preconditioner similar to the proposal in S. Olver and Townsend 2013 to improve the conditioning to $\kappa_2(Q) = \mathcal{O}(1)$ were unsuccessful.
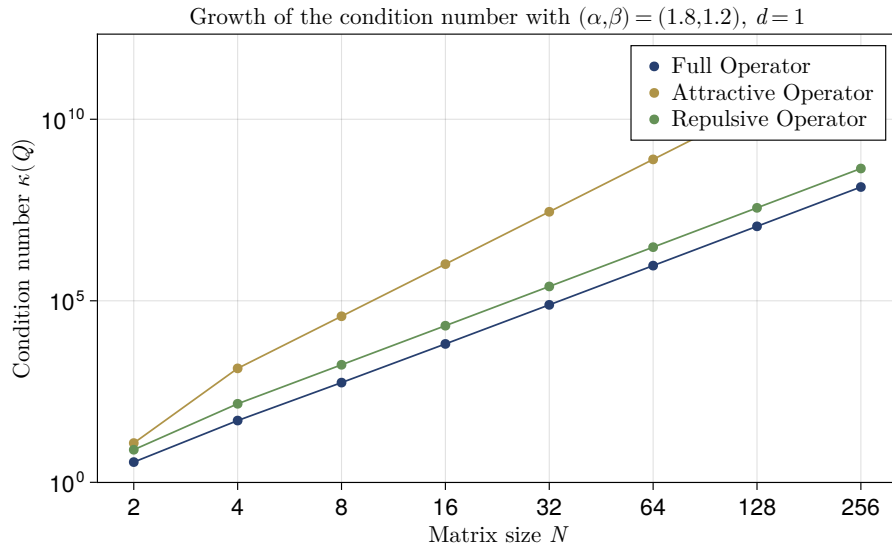
Figure 6.2: Growth of the 2-norm condition number $\kappa_2(Q)$ of the attractive-repulsive operators $Q^{(\alpha)}$, $Q^{(\beta)}$ and $Q_{\alpha,\beta}$ for growing system size N.

The improvement of coefficient decay for high orders N due to Tikhonov regularisation, as discussed in Section 4.5.1, can be seen in Figure 6.3.
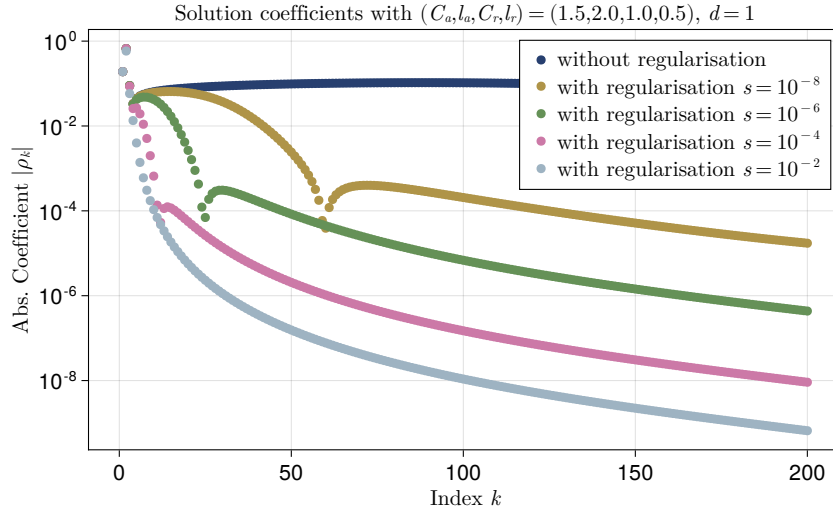
Figure 6.3: Absolute value of the solution coefficients ρ_k with and without Tikhonov regularisation after the solution of a 200×200 linear system.

6.2   Implementation Architecture

The spectral method solver is written in Julia (Bezanson et al. 2017) whereas the simulator is written in C++. To compile the simulator, please run

```
$ mkdir build; cd build/; cmake ..  -DCMAKE_BUILD_TYPE=Release
$ make -j4 in a bash terminal.
```

In order to run tests of the numerical solver implementation, run

```
$ julia solver/tests.jl
```

in a bash terminal. In order to regenerate all plots at once, including simulation output from the C++ implementation, run

```
$ julia solver/plotall.jl
```

in a terminal.

In the attractive-repulsive case, the full solution process, including the construction of the operator and solving a linear system, takes (2.68 ± 0.02) ms with a memory allocation estimate of around 2 MB, for an operator of size $N = 30$ (enough for most real-world applications). For an operator of size $N = 200$, it takes (850 ± 20) ms with a memory estimate of about 500 Mβ. In the case of the general kernel spectral method, the solution takes (3.24 ± 0.03) ms for $N = 30$. For $N = 200$, it takes (970 ± 36) ms. Both require a similar amount of memory as in the attractive-repulsive case. These benchmarks were accumulated on an Intel ® i7-5600U CPU running at 2.6 GHz, as the average over 50 individual runs.

7
Conclusion

In the present thesis, we explored the surprisingly complex behaviour of many-body systems arising from simple pairwise particle-particle interactions and, in some cases, self-propulsion and friction terms. For certain types of interactions, these systems approach equilibrium distributions $\hat{\rho}(\boldsymbol{x})$ which we aim to solve for using a spectral method, assuming their radial symmetry (a natural supposition in the absence of an external potential).

After introducing some theory in Chapter 2 and setting up a particle simulator to verify our findings in Chapter 3, we constructed a spectral method for power law interaction potentials in Chapter 4 based on Jacobi polynomials. The resulting spectral method is a highly efficient direct method with excellent convergence properties and solvability due to the banded operators appearing in it. As an original extension, we introduced a numerical method for constructing the spectral solution for general kernels $K(r)$ in Chapter 5. The solutions obtained by the general kernel spectral method match the results from particle simulations. Both methods reproduce analytical solutions to arbitrary precision and provide solutions for cases in which analytical solutions are unknown. Finally, we compared the numerical solution in the continuous situation with particle simulations in Chapter 6.

Next to the written part, the reader will find an implementation of the particle simulator written in C++ online (Waldert 2023), including a GUI, as well as the spectral method solver written in Julia.

Acronyms, Definitions and Theorems

Definitions

Theorems

Lemmata

Remarks

Bibliography

Akita, Kiyomi and Fumitake Yoshida (Jan. 1973). 'Gas Holdup and Volumetric Mass Transfer Coefficient in Bubble Columns. Effects of Liquid Properties'. In: *Ind. Eng. Chem. Process Des. Dev.* 12.1, pp. 76–80. ISSN: 0196-4305. DOI: 10.1021/i260045a015.

Arora, Manmohan S. and S. D. Bajpai (Jan. 1995). 'A new proof of the orthogonality of Jacobi polynomials'. In: *Demonstratio Math.* 28.1, pp. 177–180. ISSN: 2391-4661. DOI: 10.1515/dema-1995-0122.

Bezanson, Jeff, Alan Edelman, Stefan Karpinski and Viral B Shah (2017). 'Julia: A fresh approach to numerical computing'. In: *SIAM Review* 59.1, pp. 65–98. DOI: 10.1137/141000671.

Biler, Piotr, Cyril Imbert and Grzegorz Karch (June 2011). 'Barenblatt profiles for a nonlocal porous medium equation'. In: *C. R. Math.* 349.11, pp. 641–645. ISSN: 1631-073X. DOI: 10.1016/j.crma.2011.06.003.

Carrillo, José Antonio, Young-Pil Choi and Maxime Hauray (2014). 'The derivation of swarming models: Mean-field limit and Wasserstein distances'. In: *Collective Dynamics from Bacteria to Crowds: An Excursion Through Modeling, Analysis and Simulation.* Wien, Austria: Springer, Vienna, pp. 1–46. ISBN: 978-3-7091-1785-9. DOI: 10.1007/978-3-7091-1785-9_1.

Carrillo, José Antonio and Yanghong Huang (2017). 'Explicit equilibrium solutions for the aggregation equation with power-law potentials'. In: *Kinetic and Related Models* 10.1, pp. 171–192. ISSN: 1937-5093. DOI: 10.3934/krm.2017007.

Carrillo, José Antonio, Yanghong Huang and S. Martin (Oct. 2014). 'Explicit flock solutions for Quasi-Morse potentials'. In: *Eur. J. Appl. Math.* 25.5, pp. 553–578. ISSN: 0956-7925. DOI: 10.1017/S0956792514000126.

Carrillo, José Antonio and Ruiwen Shu (Nov. 2022). 'From radial symmetry to fractal behavior of aggregation equilibria for repulsive–attractive potentials'. In: *Calc. Var. Partial Differential Equations* 62.1, pp. 28–61. ISSN: 1432-0835. DOI: 10.1007/s00526-022-02368-4.

Cavagna, Andrea, Alessio Cimarelli, Irene Giardina, Giorgio Parisi, Raffaele Santagati, Fabio Stefanini and Massimiliano Viale (June 2010). 'Scale-free correlations in

starling flocks'. In: *Proc. Natl. Acad. Sci. U.S.A.* 107.26, pp. 11865–11870. DOI: 10.1073/pnas.1005766107.

Cipra, Barry A (2000). 'The best of the 20th century: Editors name top 10 algorithms'. In: *SIAM news* 33.4, pp. 1–2. URL: https://archive.siam.org/pdf/news/637.pdf (visited on 14/08/2023).

D'Orsogna, M. R., Y. L. Chuang, A. L. Bertozzi and L. S. Chayes (Mar. 2006). 'Self-Propelled Particles with Soft-Core Interactions: Patterns, Stability, and Collapse'. In: *Phys. Rev. Lett.* 96.10, p. 104302. ISSN: 1079-7114. DOI: 10.1103/PhysRevLett.96.104302.

D'Orsogna, Maria R. (Dec. 2017). *Why do animals form swarms?* URL: https://ed.ted.com/lessons/why-do-animals-form-swarms-maria-r-d-orsogna (visited on 12/08/2023).

Danisch, Simon and Julius Krumbiegel (2021). 'Makie.jl: Flexible high-performance data visualization for Julia'. In: *Journal of Open Source Software* 6.65, p. 3349. DOI: 10.21105/joss.03349.

Favard, Jean (1935). 'Sur les polynômes de Tchebicheff'. French. In: *Comptes Rendus Hebdomadaires des Séances de l'Académie des Sciences, Paris* 200. zbMath: 0012.06205, pp. 2052–2053. ISSN: 0001-4036.

Greengard, L. and V. Rokhlin (Dec. 1987). 'A fast algorithm for particle simulations'. In: *J. Comput. Phys.* 73.2, pp. 325–348. ISSN: 0021-9991. DOI: 10.1016/0021-9991(87)90140-9.

Gutleb, Timon S., José Antonio Carrillo and Sheehan Olver (Dec. 2022a). 'Computation of Power Law Equilibrium Measures on Balls of Arbitrary Dimension'. In: *Constr. Approx.*, pp. 1–46. ISSN: 1432-0940. DOI: 10.1007/s00365-022-09606-0.

– (Sept. 2022b). 'Computing equilibrium measures with power law kernels'. In: *Math. Comput.* 91.337, pp. 2247–2281. ISSN: 0025-5718. DOI: 10.1090/mcom/3740.

Hoerl, Arthur E. and Robert W. Kennard (Feb. 1970). 'Ridge Regression: Biased Estimation for Nonorthogonal Problems'. In: *Technometrics* 12.1, pp. 55–67. ISSN: 0040-1706. DOI: 10.1080/00401706.1970.10488634.

Huang, Yanghong (Aug. 2014). 'Explicit Barenblatt profiles for fractional porous medium equations'. In: *Bull. London Math. Soc.* 46.4, pp. 857–869. ISSN: 0024-6093. DOI: 10.1112/blms/bdu045.

Kwaśnicki, Mateusz (Feb. 2017). 'Ten Equivalent Definitions of the Fractional Laplace Operator'. In: *FCAA* 20.1, pp. 7–51. ISSN: 1314-2224. DOI: 10.1515/fca-2017-0002.

Liu, Dong C. and Jorge Nocedal (Aug. 1989). 'On the limited memory BFGS method for large scale optimization'. In: *Math. Program.* 45.1, pp. 503–528. ISSN: 1436-4646. DOI: 10.1007/BF01589116.

Magnus, Wilhelm, Fritz Oberhettinger, R. P. Soni and Eugene P. Wigner (Dec. 1967). 'Formulas and Theorems for the Special Functions of Mathematical Physics'. In: *Phys. Today* 20.12, pp. 81–83. ISSN: 0031-9228. DOI: 10.1063/1.3034082.

Michel, N. and M. V. Stoitsov (Apr. 2008). 'Fast computation of the Gauss hypergeometric function with all its parameters complex with application to the Pöschl–Teller–Ginocchio potential wave functions'. In: *Comput. Phys. Commun.* 178.7, pp. 535–551. ISSN: 0010-4655. DOI: 10.1016/j.cpc.2007.11.007.

Milne-Thomson, L. M. (Aug. 1945). *A Treatise on the Theory of Bessel Functions.* Vol. 156. 3955. Nature Publishing Group. DOI: 10.1038/156190a0.

Mogensen, Patrick Kofod et al. (Aug. 2023). 'JuliaNLSolvers/Optim.jl: v1.7.7'. In: *Zenodo.* DOI: 10.5281/zenodo.8254057.

Nelder, J. A. and R. Mead (Jan. 1965). 'A Simplex Method for Function Minimization'. In: *Comput. J.* 7.4, pp. 308–313. ISSN: 0010-4620. DOI: 10.1093/comjnl/7.4.308.

Olver, F.W.J., A.B.O. Daalhuis, D.W. Lozier, B.I. Schneider, R.F. Boisvert, C.W. Clark, B.R. Miller and B. V. Saunders (Dec. 2018). *NIST Digital Library of Mathematical Functions.* https://dlmf.nist.gov. DOI: 10.1023/A:1022915830921. (Visited on 18/08/2023).

Olver, Sheehan, Timon Salar Gutleb, Ioannis Papadopoulos and Julia TagBot (May 2023). 'JuliaApproximation/EquilibriumMeasures.jl: v0.1.0'. In: *Zenodo.* DOI: 10.5281/zenodo.7898851.

Olver, Sheehan and Alex Townsend (Aug. 2013). 'A Fast and Well-Conditioned Spectral Method'. In: *SIAM Review.* DOI: 10.1137/120865458.

Pearson, John W., Sheehan Olver and Mason A. Porter (Mar. 2017). 'Numerical methods for the computation of the confluent and Gauss hypergeometric functions'. In: *Numer. Algorithms* 74.3, pp. 821–866. ISSN: 1572-9265. DOI: 10.1007/s11075-016-0173-0.

Prudnikov, A.P., Y.A. Brychkov, I.U.A. Brychkov and O.I. Marichev (1986). *Integrals and Series: More special functions.* Integrals and Series. Gordon and Breach Science Publishers. ISBN: 9782881246821.

Schönlieb, C.-B. (2015). *Numerical Analysis - Lecture 11*. Mathematical Tripos Part II: Michaelmas Term 2015. URL: https://www.damtp.cam.ac.uk/user/cbs31/Teaching_files/c11.pdf (visited on 23/08/2022).

Slevinsky, Richard Mikael (July 2023). 'Fast and stable rational approximation of generalized hypergeometric functions'. In: *arXiv*. Preprint. DOI: 10.48550/arXiv.2307.06221.

Sorensen, D. C. (1982). 'Newton's Method with a Model Trust Region Modification'. In: *SIAM Journal on Numerical Analysis* 19.2, pp. 409–426. DOI: 10.1137/0719026.

Trefethen, Lloyd N. (2019). *Approximation Theory and Approximation Practice, Extended Edition*. Philadelphia, PA: Society for Industrial and Applied Mathematics. DOI: 10.1137/1.9781611975949.

Vicsek, Tamás, András Czirók, Eshel Ben-Jacob, Inon Cohen and Ofer Shochet (Aug. 1995). 'Novel Type of Phase Transition in a System of Self-Driven Particles'. In: *Phys. Rev. Lett.* 75.6, pp. 1226–1229. ISSN: 1079-7114. DOI: 10.1103/PhysRevLett.75.1226.

Waldert, Peter (Aug. 2023). *General Kernel Spectral Methods for Equilibrium Measures*. Version 0.0.1. DOI: 10.5281/zenodo.8289989. URL: https://github.com/MrP01/Dissertation (visited on 30/08/2023).

Wolfram Functions (29th Oct. 2001). *Pochhammer symbol: Representations through equivalent functions*. Wolfram Functions: 06.10.27.0003.01. Wolfram Research, Inc.

Yoshida, Masaaki (1997). *Hypergeometric Functions, My Love*. Wiesbaden, Germany: Vieweg+Teubner Verlag. ISBN: 978-3-322-90166-8. DOI: 10.1007/978-3-322-90166-8.

List of Figures

Appendix A – Exploring the Energy Function

In an attempt to find an explicit expression of the energy function $E(\alpha, \beta, R, d)$, we plotted and fitted the energy function in α and R so that it can be visualised with $d = 1$ and $\beta = 0.4$ held constant.

The fit of $E(\alpha, R)$ depicted in Figure A.1 is done by minimising the square error between energy values returned by the solver and the following function:

$$E(\alpha, R; \boldsymbol{x}) = x_1 + \alpha \cdot x_2 + \alpha^2 \cdot x_3 + \alpha^3 \cdot x_4 + R^\alpha \cdot x_5 + R^\beta \cdot x_6$$
$$+ R \cdot x_7 + R^2 \cdot x_8 + R^3 \cdot x_9 + R^4 \cdot x_{10} + \log(\alpha) \cdot x_{11}.$$

The resulting best-fit parameter combination is

$$\boldsymbol{x}_{\min} = (-3.22, 4.19, -0.99, 0.11, -0.15, -1.91, 0.13, 0.66, -0.13, -0.03, -3.18)^T.$$

as obtained through Optim.jl's LBFGS minimisation routine (Mogensen et al. 2023) with AD for the gradient.
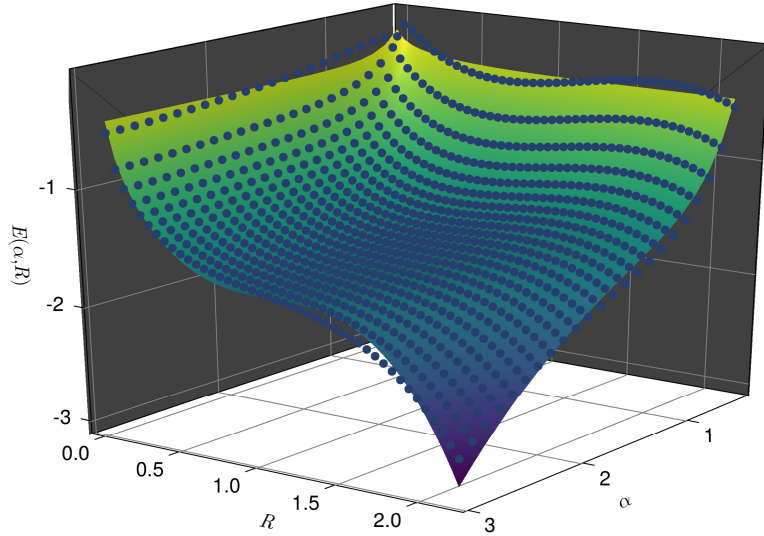

Figure A.1: Surface plot of the total potential energy $E(\alpha, R)$, the blue scatter points represent the fit $E(\alpha, R; \boldsymbol{x}_{\min})$.

The conclusion seems to be that the behaviour is highly non-polynomial, even when using powers R^α and R^β, etc. instead of only monomials. One could expect this given the analytical energy expressions in Section 2.7 and Carrillo and Huang 2017. Even adding in some of the terms $(B(\cdot, \cdot) \cdot \cos(\cdot)$, etc.) from the analytical expressions did not help. We also tried higher orders in α, R, more log terms, cross-terms, and we even experimented with the beta function.

Appendix B – Various Plots

Figure B.1 depicts a "bump" solution resulting from an attractive-repulsive interaction kernel. The pseudo energy dependence on position $\boldsymbol{x}$ (and due to radial symmetry, on r) for different support radii R is given in Figure B.2. Instead of taking energy as the average $\overline{I}_{m,n}^{(\alpha,\beta)}$, one can use $I_{m,n}^{(\alpha,\beta)}(\boldsymbol{x})$. Figure B.3 illustrates the effects of various parameters in the attractive-repulsive case.
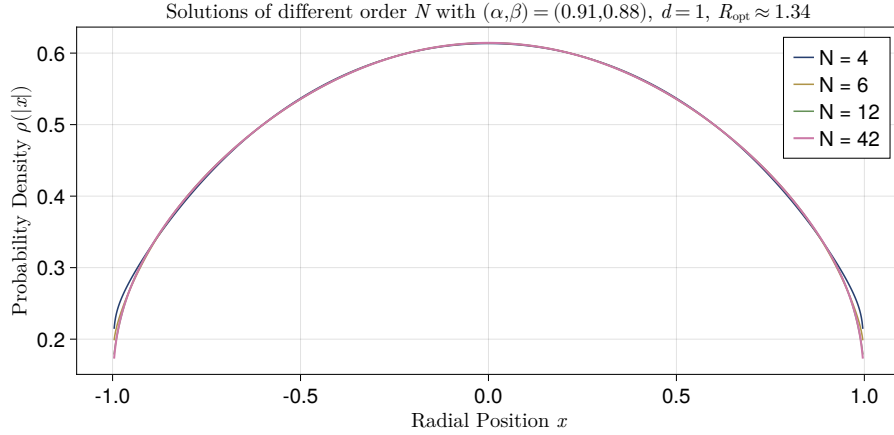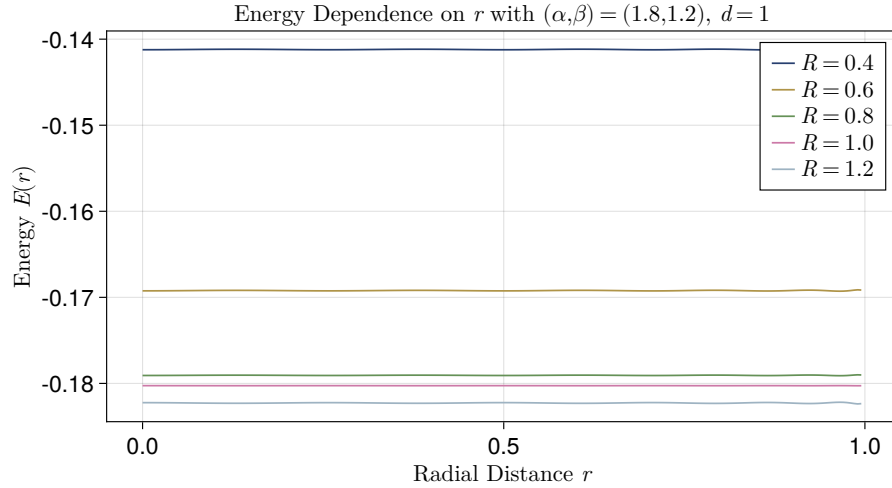

Figure B.1: Solutions with bump parameters.

Figure B.2: Plot of the spatial energy dependence on r, for different values of the domain support radius R. As one can see, $\tilde{E}(\boldsymbol{x}) = \sum_{k=0}^{N-1} \rho_k I_{m,n}^{(\alpha,\beta)}(\boldsymbol{x})$ is roughly constant and this figure is only present as visual proof to increase our confidence in the construction of the spectral method.
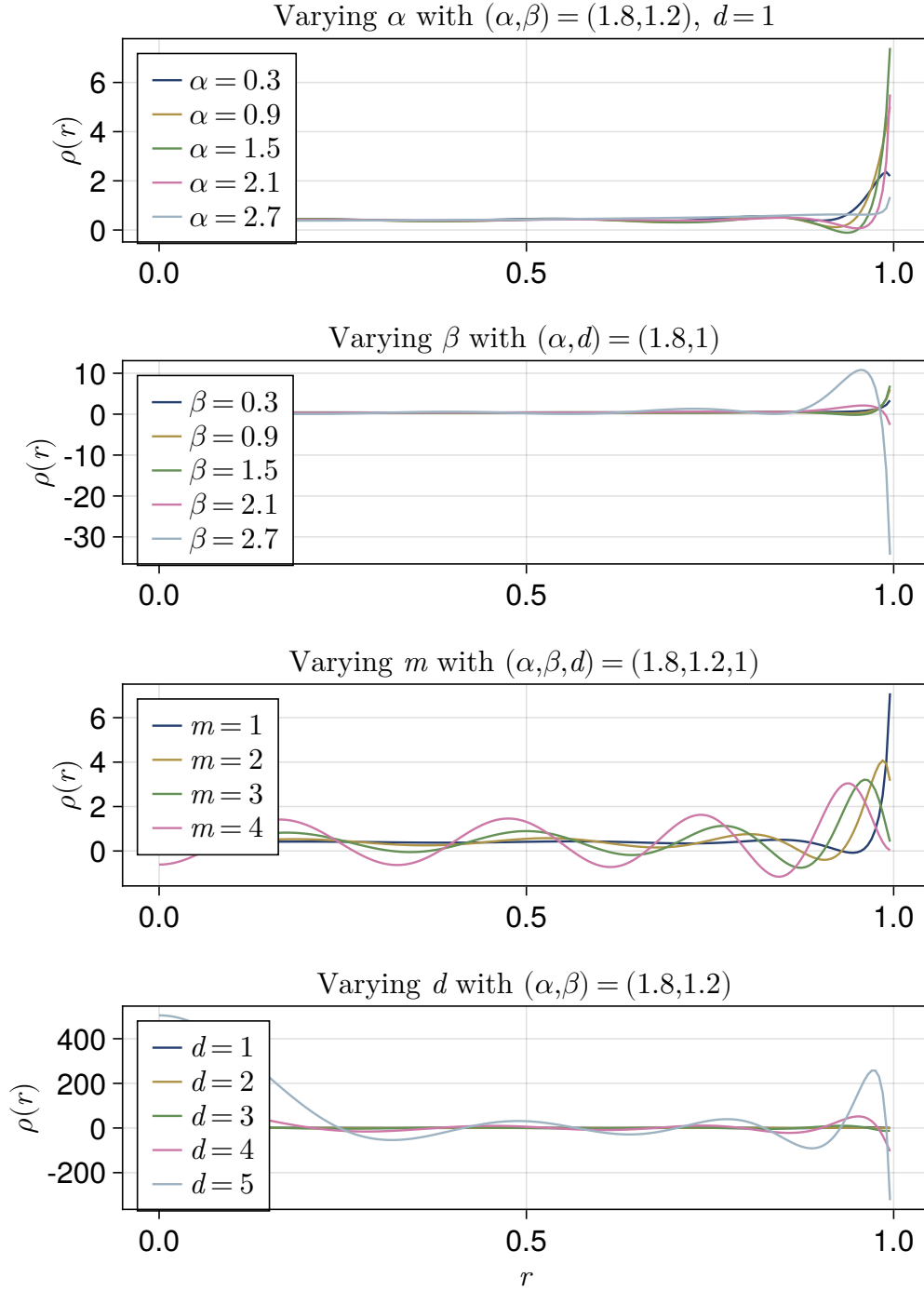
Figure B.3: Varying different parameters in the solver to demonstrate their effect. See also, Figure 5.5.

Appendix C – Code Snippets

C.1   Leapfrog Integration

```cpp
void ParticleBox::simulate(size_t timesteps) {
  double afterAccelerations[PARTICLES][DIMENSION];
  f(afterAccelerations);
  for (size_t t = 0; t < timesteps; t++) {
    ParticleVectors beforeAccelerations = afterAccelerations;
    memcpy(beforeAccelerations, afterAccelerations, PARTICLES *
     DIMENSION * sizeof(double));
    for (size_t i = 0; i < PARTICLES; i++) {
      for (size_t d = 0; d < DIMENSION; d++)
        positions[i][d] += p.tau * velocities[i][d] + square(p.tau) /
     2 * beforeAccelerations[i][d];
    }

    f(afterAccelerations);
    for (size_t i = 0; i < PARTICLES; i++) {
      for (size_t d = 0; d < DIMENSION; d++) {
        velocities[i][d] += (p.tau / 2 * (beforeAccelerations[i][d] +
     afterAccelerations[i][d])) / p.boxScaling;
      }
    }
    reflectParticles();
  }
}
```

C.2 Operator Construction without Recurrence

```julia
OpMem = LRUCache.LRU{Tuple{Int64, Float64,SolutionEnvironment},
↪  Matrix{BigFloat}}(maxsize=20)
"""Creates a power-law operator given alpha and beta. Caches it."""
function constructOperator(N::Int64, beta::Float64,
↪  env::SolutionEnvironment)::Matrix{BigFloat}
  get!(OpMem, (N, beta, env)) do
    Mat = zeros(BigFloat, N, N)
    r_axis = axes(env.P, 1)
    for n in 0:N-1
      Function = Utils.theorem216.(r_axis; n=n, beta=beta, p=env.p)
      ExpansionCoeffs = env.P[:, 1:N] \ Function  # expands the
        ↪  function in the P basis
      Mat[:, n+1] .= ExpansionCoeffs
    end
    Utils.zeroOutTinyValues!(Mat)
    Mat
  end
end
```